Quantifying magma overpressure beneath a submarine caldera: A mechanical modeling approach to tsunamigenic trapdoor faulting near Kita-Ioto Island, Japan

Osamu Sandanbata[1,2†], and Tatsuhiko Saito[1]

[1] National Research Institute for Earth Science and Disaster Resilience, Ibaraki, Japan.

[2] *Now at* Earthquake Research Institute, the University of Tokyo, Tokyo, Japan.

Corresponding author: Osamu Sandanbata (osm3@eri.u-tokyo.ac.jp)

Key Points (<140 characters):

- Non-double-couple earthquakes with seismic magnitudes of 5.2–5.3 recurred in the vicinity of a submarine caldera near Kita-Ioto Island.
- A mechanical model of trapdoor faulting based on tsunami data of the 2008 earthquake infers pre-seismic overpressure in a magma reservoir.
- Uncertainty in fault geometry varies our estimate of pre-seismic overpressure (5–20 MPa) and co-seismic pressure drop ratio (10–40 %).

Abstract

Submarine volcano monitoring is vital for assessing volcanic hazards but challenging in remote and inaccessible environments. In the vicinity of Kita-Ioto Island, south of Japan, unusual M~5 non-double-couple volcanic earthquakes exhibited quasi-regular recurrence near a submarine caldera. Following the earthquakes in 2008 and 2015, a distant ocean bottom pressure sensor recorded distinct tsunami signals. In this study, we aim to find a source model of the tsunami-generating earthquake and quantify the pre-seismic magma overpressure within the caldera's magma reservoir. Based on the earthquake's characteristic focal mechanism and efficient tsunami generation, we hypothesize that submarine trapdoor faulting occurred due to highly pressurized magma. To investigate this hypothesis, we establish mechanical earthquake models that link pre-seismic magma overpressure to the size of the resulting trapdoor faulting, by considering stress interaction between a ring-fault system and a reservoir of the caldera. The trapdoor faulting with large fault slip due to magma-induced shear stress in the submarine caldera reproduces well the observed tsunami waveform. Due to limited data, uncertainties in the fault geometry persist, leading to variations of magma overpressure estimation: the pre-seismic magma overpressure ranging approximately from 5 to 20 MPa, and the co-seismic pressure drop ratio from 10 to 40 %. Although better constraints on the fault geometry are required for robust magma pressure quantification, this study shows that magmatic systems beneath calderas are influenced significantly by intra-caldera fault systems and that tsunamigenic trapdoor faulting provides rare opportunities to obtain quantitative insights into remote submarine volcanism hidden under the ocean.

Plain Language Summary

Monitoring submarine volcanoes is essential to understand and prepare for potential volcanic hazards in/around oceans, but it's challenging because these volcanoes are located in inaccessible environments. In a submarine volcano with a caldera structure in south of Japan, unusual volcanic earthquakes took place every several years. After one of these earthquakes in 2008, a pressure sensor deployed on the sea bottom recorded a clear signal of tsunami waves. By utilizing the tsunami signal from the earthquake, we attempt to measure how much magma pressure was building up beneath the volcano before the earthquake. Assuming that the

earthquake happened with sudden rupture on an intra-caldera fault system due to highly pressurized magma beneath the volcano, we develop a method to assess the built-up magma pressure through quantification of the earthquake and tsunami sizes. By applying the method, we estimate that the volcanic edifice was under a highly stressed condition before the earthquake, suggesting active magma accumulation process that has continued beneath the volcano. Signals emitted from volcanic earthquakes under oceans shed light on the activity of poorly monitored submarine volcanoes.

1 Introduction

Investigation of the magma pressure beneath volcanoes is important for forecasting eruptions and assessing their eruption potential. The overpressure of magma, or the excess magma pressure relative to the stress in the surrounding host rock, induces diverse volcanic unrest, such as deformation, seismicity, or gas emission, potentially triggering a volcanic eruption when the pressure exceeds the strength of the host rock (Sparks, 2003). Previous studies have tried to detect signals of volcanic unrest to examine the magma pressure and/or the stress state of the host rock (Anderson et al., 2019; Gregg et al., 2018; Le Mével et al., 2016; Massa et al., 2016; Segall & Anderson, 2021). Recently, mechanics-based numerical models have been developed to establish links between magma overpressure to surface deformation observed by on-site instruments and/or satellites. These models helped to quantify the sub-surface pressure/stress state, tracking the change over time leading up to eruptions (Cabaniss et al., 2020; Gregg et al., 2022; Segall & Anderson, 2021). These previous studies provided quantitative insights into the eruption triggering due to the magma overpressure. Thus, magma pressure or stress status in volcanoes can be vital proxies for assessing the potentials and the timings of eruptions.

Submarine volcanoes have the potential to bring severe damage to local and even global societies with volcanic tsunamis, as highlighted by recent tsunami events related to the 15 January 2022 eruption of Hunga Tonga-Hunga Ha'apai, Tonga (e.g., Kubota et al., 2022; Lynett et al., 2022; Purkis et al., 2023; Borrero et al., 2023; Kubo et al., 2022), or the 22 December 2018 eruption of Anak Krakatau, Indonesia (e.g., Grilli et al., 2019; Muhari et al., 2019; Heidarzadeh, Ishibe, et al., 2020; Heidarzadeh, Putra et al., 2020; Mulia et al., 2020; Ye et al., 2020), and by historical events listed in Day (2015) and Paris et al. (2014), some of which caused over hundreds to thousands of fatalities. Yet, it is often challenging to investigate submarine volcanoes due to the lack of on-site monitoring systems. Many previous studies remotely detected geophysical signals from submarine volcanoes, such as, seawater acoustic waves (Metz et al., 2016; Tepp & Dziak, 2021), seismic waves (Cesca et al., 2020; Saurel et al., 2021; Sugioka et al., 2001), or tsunami waves (Fukao et al., 2018; Sandanbata et al., 2018; Y. Wang et al., 2019), shedding light on volcanic processes in submarine volcanoes. However, only a limited number of studies have utilized these remote signals to examine the magma pressure or the stress state of submarine volcanoes.

In this paper, we aim to investigate the magma overpressure and the stress status in a submarine caldera near Kita-Ioto Island, south of Japan, by studying a volcanic earthquake driven by the sub-caldera magma accumulation. We first report volcanic earthquakes with seismic magnitudes of M_w~5 that recurred near the caldera, and show that one of the earthquakes in 2008 caused a tsunami that traveled in the ocean over the distance of about 1,000 km. We then develop a mechanical model of the earthquake to quantitatively link the sub-caldera magma overpressure to the earthquake size and thereby the tsunami size. By combining the tsunami waveform data with the mechanical model, we estimate the magma overpressure that drove the volcanic earthquake, as well as explain the tsunami generation. We discuss the variation in our magma overpressure estimate, the comparison with previous studies, the model validation with seismic data, the trapdoor faulting recurrence, and the limitation of our proposed modeling approach, and conclude by highlighting the significant potential of studying submarine trapdoor faulting for remote quantification of caldera volcanism in the ocean.

2 Tsunami signal from a volcanic earthquake at Kita-Ioto submarine caldera

Kita-Ioto Island is an inhabited island in the Izu-Bonin Arc, to the northwest of which a submarine caldera with a size of 12 km x 8 km is located, hereafter called *Kita-Ioto caldera* (Figures 1a–1c). While no historical eruption on the island has been reported, past submarine eruptions were found at a submarine vent called *Funka Asane* on a major cone within the caldera structure (Figure 1c). According to Japan Meteorological Agency (2013), the latest eruptions of Funka Asane were reported between 1930 to 1945, and its volcanic activity has been recently inferred from sea-color changes and underwater gas emission near the vent (Ossaka et al., 1994). In March 2022, Japan Meteorological Agency (2022) reported ash-like clouds near Kita-Ioto

Island and suggested the possibility of an eruption, but it is not clear whether the clouds were caused by an eruption or by meteorological factors. Thus, the volcanic activity of the submarine caldera has not been understood well.

Active volcanism of Kita-Ioto caldera shows unique seismic activity characterized by shallow earthquakes near the caldera repeating every 2–5 years, in 2008, 2010, 2015, 2017, and 2019, in addition to that in 1992 (Figure 1c; Table S1). As the focal mechanism of the earthquake in 2008 represents in Figure 1c, these six earthquakes reported in the Global Centroid Moment Tensor (GCMT) catalog (Ekström et al., 2012) similarly had seismic magnitudes of M_w 5.2–5.3 and non-double-couple moment tensors with large compensated-linear-vector-dipole (CLVD) components (Figure S1). Such types of earthquakes at a shallow depth in volcanic or geothermal environments are often called vertical-CLVD earthquakes (e.g., Shuler, Nettles, & Ekström, 2013; Sandanbata, Kanamori, et al., 2021), which can be categorized into two types: *vertical-T CLVD earthquakes* with a nearly vertical tension and *vertical-P CLVD earthquakes* with a nearly vertical pressure axis. In recent caldera studies, vertical-T earthquakes were observed in caldera inflation phases (Bell et al., 2021; Glastonbury-Southern et al., 2022; Jónsson, 2009; Sandanbata et al., 2021), whereas vertical-P earthquakes coincided with caldera collapse and formation (Gudmundsson et al., 2016; Lai et al., 2021; Michon et al., 2007; Riel et al., 2015; Rodríguez-Cardozo et al., 2021). The earthquakes near Kita-Ioto caldera fall into the vertical-T type, implying their association with the caldera inflation.

Yet, the mechanisms of shallow vertical-CLVD earthquakes are often indistinguishable only from the seismic characters, due to weak constraint on parts of moment tensor components ($M_{r\theta}$ and $M_{r\phi}$) (Kanamori & Given, 1981; Sandanbata, Kanamori, et al., 2021) and a tradeoff between the vertical-CLVD and isotropic components (Kawakatsu, 1996). These ambiguities leave room for different interpretations for the earthquake mechanism, such as fault slips in calderas, deformation of a magma reservoir, or volume change due to heated fluid injection, as previously proposed for similar vertical-CLVD earthquakes (Shuler, Ekström, & Nettles, 2013, and references therein).

Following the earthquake that occurred at 13:10 on 12 June 2008 (UTC), a tsunami-like signal was recorded by an ocean-bottom-pressure (OBP) gauge with a sampling interval of 15 s of the station 52404, ~1,000 km away from the caldera, of Deep-ocean Assessment and

Reporting of Tsunamis (DART) system (Bernard & Meinig, 2011) (Figure 1a). Figure 1d shows the OBP data, which we obtain by removing the tidal component from and by applying the bandpass (2–10 mHz) Butterworth filter to the raw record. The OBP data demonstrates that clear oscillations with the maximum pressure of ~2 mm H_2O started ~5,000 s after the earthquake origin time. Our calculation using the Geoware TTT (Tsunami Travel Time) software (Geoware, 2011) estimates that the tsunami would have arrived ~5,050 s after the origin time (Figure S2), if a tsunami was generated in the center of Kita-Ioto caldera at the earthquake timing. The estimated tsunami arrival time agrees well with the timing when the oscillation starts in the OBP record (Figure 1d). Our spectrogram analysis for the OBP waveform record (Figure S3) shows that lower-frequency oscillations, starting around the estimated tsunami arrival time, are followed by higher-frequency signals. This frequency-dependent character with later arrivals of higher-frequency components is typical for tsunami waves with the dispersion that traveled over long distances (e.g., Saito et al., 2010; Sandanbata et al., 2018). Hence, it is very likely that the OBP gauge captured a tsunami signal from the 2008 earthquake at Kita-Ioto caldera.

3 Hypothetical source mechanism

Given the tsunami generation by the vertical-T CLVD earthquake at Kita-Ioto caldera, hereafter we call *Kita-Ioto caldera earthquake*, we hypothesize the *trapdoor faulting* mechanism in the inflating caldera, or sudden slip of an intra-caldera ring fault interacting with a sill-like magma reservoir accommodating highly pressurized magma. This hypothesis is mainly from analogy with other better-studied calderas, which accompanied vertical-T CLVD earthquakes causing large caldera deformation or tsunamis. The trapdoor faulting accompanying a vertical-T CLVD earthquake of M_w~5 was first reported in a subaerial caldera of Sierra Negra volcano in the Galapagos Islands, where the phenomenon occurred several times and caused the caldera uplift of a few meters by each event (Amelung et al., 2000; Gregg et al., 2018; Jónsson, 2009; Shreve & Delgado, 2023; Zheng et al., 2022). Recently, Sandanbata et al. (2022; 2023) revealed that trapdoor faulting repeated with M_w 5.4–5.8 vertical-T CLVD earthquakes and generated large tsunamis at two submarine calderas: Sumisu caldera in the Izu-Bonin Arc (Sandanbata et al., 2022), and a submerged caldera near Curtis Island, or Curtis caldera, in the Kermadec Arc (Sandanbata et al., 2023). Those submarine earthquakes are particularly similar to the 2008 Kita-

Ioto caldera earthquake in terms of seismic and tsunami characters, and source environments in calderas.

4 Methodology

In this section, we describe the methodology to construct a 3-D mechanical model of trapdoor faulting and to apply it to the tsunami data of the 2008 Kita-Ioto caldera earthquake. Through the application, we attempt to reproduce the tsunami data and estimate the sub-caldera magma overpressure that drove the tsunamigenic earthquake.

4.1 Mechanical model of trapdoor faulting

We consider the 3-D half-space elastic medium of the host rock with an intra-caldera ring fault and a horizontal crack filled with magma (Figure 2). The ring fault and the horizontal crack are discretized into small triangular meshes, or sub-faults and sub-crack (with N_F and N_C meshes), respectively. The crack is assumed to have a finite inner volume and filled with compressible magma. Note that we do not consider viscoelasticity or heterogeneous rheology of the host rock, as the limitations are discussed later in Section 6.5.3.

We assume that trapdoor faulting is driven by magma overpressure in the crack, as follows; before trapdoor faulting, continuous magma input into the crack gradually increases the inner pressure and volume, and causes elastic stress in the host rock, accumulating shear stress on the ring fault; when the shear stress on the fault overcomes its strength, trapdoor faulting takes place. In the following, we model trapdoor faulting as a dislocation model that combines sudden and interactive processes of dip-slip on the fault with stress drop, deformation (vertical opening/closure) of the crack with volume change, and pressure change of the magma in the crack. Note that, some previous studies used the terminology of trapdoor faulting to refer to only the fault part (e.g., Amelung et al., 2000), while we consider it as the composite process involving both the fault and the magma-filled crack.

<u>Pre-seismic elastic stress in the host rock</u>

As a reference state, we consider that the magma pressure p_0 in the crack is in equilibrium with the background stress σ_{ij}^0 in the host rock due to the lithostatic and seawater loading, and that the background differential stress as zero. If we take the stress in the host rock as positive when it is compression, the background stress at an arbitrary position in the reference state is expressed as:

$$\sigma_{ij}^{0} = (\rho_h z + \rho_s H) g \delta_{ij}, \text{—} (1)$$

where ρ_h and z are the host rock density and the arbitrary depth in the host rock, respectively, ρ_s and H are the seawater density and the approximated thickness of the overlying seawater layer, respectively, g is the gravitational acceleration, and δ_{ij} is the Kronecker's delta. The magma pressure in the reference state is expressed as follows:

$$p_0 = (\rho_h z_0 + \rho_s H) g. \text{—} (2)$$

where z_0 is the depth of the horizontal crack, respectively.

We assume that long-term magma input into the crack increases the magma overpressure and opens the crack vertically, and that the resultant crack deformation changes the stress in the host rock. Thus, the shear stress is accumulated on the fault, which eventually causes trapdoor faulting. Magma pressure in the pre-seismic state, just before trapdoor faulting, is assumed to be spatially uniform within the crack and expressed as $p = p_0 + p_e$, where p_e is the pre-seismic magma overpressure. If we denote the spatial distribution of the crack opening in the pre-seismic state as $\underline{\delta_e}$, the equilibrium relationship between the normal stress on the surfaces of sub-cracks and the inner magma pressure reduces to:

$$\underline{\sigma_e} = P\underline{\delta_e} = p_e \underline{I_C}, \text{—} (3)$$

where $\underline{\sigma_e}$ is the $N_C \times 1$ column vector of the pre-seismic normal stress on sub-cracks, P is the interaction matrix, with a size of $N_C \times N_C$, that map the tensile opening of sub-cracks into the normal stress on sub-cracks, and $\underline{I_C}$ is the $N_C \times 1$ column vector of ones. The distribution of the crack opening in the pre-seismic state $\underline{\delta_e}$ can be obtained from the second equality of Equation 3. Then, the pre-seismic shear stress along the dip direction on the surfaces of sub-faults (denoted as $\underline{\tau_e}$) created by the magma overpressure p_e can be expressed as:

$$\underline{\tau_e} = Q\underline{\delta_e}, \text{—} (4)$$

where Q is the interaction matrix, with a size of $N_F \times N_C$, that maps the tensile opening of sub-cracks into the shear stress on sub-faults. With Equation 3, Equation 4 can be rewritten as:

$$\underline{\tau}_e = p_e\left(QP^{-1}\underline{I}_C\right). \text{— (5)}$$

The part in the bracket, $QP^{-1}\underline{I}_C$, represents the shear stress on the surfaces of sub-faults due to unit magma overpressure. If we denote it as $\underline{\hat{\tau}_e}$, Equation 5 can be rewritten as:

$$\underline{\tau}_e = p_e\underline{\hat{\tau}_e}. \text{— (6)}$$

Occurrence of trapdoor faulting

Trapdoor faulting is caused by sudden stress drop of the shear stress accumulated on the fault. The motion involves dip-slip of the fault, and deformation (opening/closure) of the crack. To determine the motion of trapdoor faulting, we here derive two boundary conditions on the surfaces of the ring fault and the horizontal crack.

Assuming that the shear stress along the dip direction on the fault decreases by a stress drop ratio α due to trapdoor faulting, the boundary condition on the surface of the fault can be expressed as:

$$\underline{\Delta\tau} = Q\underline{\delta} + R\underline{s} = -\alpha\underline{\tau}_e, \text{— (7)}$$

where $\underline{\Delta\tau}$ is the $N_F\times 1$ column vector of the shear stress change on sub-faults during trapdoor faulting. Q and R, with sizes of $N_F\times N_C$ and $N_F\times N_F$, map dip-slip of sub-faults into the normal stress on sub-crack and the shear stress on sub-faults, respectively (Q is the same as that in Equation 4).

Sudden stress change in the host rock due to dip-slip of the fault interactively accompanies deformation (opening/closure) of the crack, and the resultant normal stress change on the crack induces horizontal movement of the inner magma. For simplicity, we assume that the magma movement finishes and the magma pressure becomes spatially uniform in the crack quickly. Under this simplification, the boundary condition on the surface of the horizontal crack is derived from the equilibrium relationship between the normal stress on sub-cracks and the inner magma pressure, as follows:

$$\underline{\Delta\sigma} = P\underline{\delta} + U\underline{s} = (\Delta p)\underline{I}_c, \text{— (8)}$$

where $\underline{\Delta\sigma}$ and Δp are the $N_C\times 1$ column vector of the normal stress change on sub-cracks and the scalar of the magma pressure change during trapdoor faulting, respectively. P and U are the interaction matrices, with sizes of $N_C \times N_C$ and $N_C \times N_F$, that map the tensile opening of sub-cracks into the normal stress on sub-cracks and into the shear stress on sub-faults, respectively (P is the same as that in Equation 3).

The magma pressure change Δp during trapdoor faulting can be related to the crack volume change ΔV through the mass conservation law, as follows:

$$\Delta m/\rho_m = V_0\beta_m\Delta p + \Delta V, \text{— (9)}$$

where Δm is the magma influx and β_m is the compressibility of magma. Since previously observed trapdoor faulting occurred within less than ~10 s (Geist et al., 2008; Sandanbata et al., 2022, 2023), we can disregard magma mass influx during trapdoor faulting to reduce Equation 9 to:

$$\Delta p = -\frac{1}{\beta_m V_0}\Delta V = -\frac{1}{\beta_m V_0}\underline{A}^T\underline{\delta} = -\frac{1}{\beta_m V_0}\sum_{k=1}^{N_c} A_k\delta_k, \text{— (10)}$$

where $\underline{A}$ is the $N_C \times 1$ column vector of the areas of sub-cracks.

By substituting Equations 6 and 10 into Equations 7 and 8, respectively, we obtain the following equations:

$$\begin{bmatrix} P & U \\ Q & R \end{bmatrix}\begin{bmatrix} \underline{\delta} \\ \underline{s} \end{bmatrix} = \begin{bmatrix} \left(-\frac{1}{\beta_m V_0}\underline{A}^T\underline{\delta}\right)\underline{I_C} \\ -\alpha p_e\underline{\hat{\tau}_e} \end{bmatrix}. \text{— (11)}$$

Equation 11 can be rewritten by:

$$\begin{bmatrix} P' & U \\ Q & R \end{bmatrix}\begin{bmatrix} \underline{\delta} \\ \underline{s} \end{bmatrix} = p_e\begin{bmatrix} \underline{0} \\ -\alpha\underline{\hat{\tau}_e} \end{bmatrix}, \text{— (12)}$$

where

$$P' = P + \frac{1}{\beta_m V_0}\underline{A}^T \text{ (or } P'_{ij} = P_{ij} + \frac{1}{\beta_m V_0}A_j\text{). — (13)}$$

Equations 12 and 13 represent $N_C + N_F$ equations with $N_C + N_F$ unknown values ($\underline{\delta}$, $\underline{s}$), if we priorly assume the pre-seismic magma overpressure p_e, the stress drop ratio α, the source geometry determining the interaction matrices, and the parameters β_m and V_0. In this study, the source geometry and the parameters are assumed as described in Section 4.2. Also, the stress drop ratio is simply assumed as α = 1; in other words, the pre-seismic shear stress on the fault completely vanishes to zero due to trapdoor faulting. In this case, Equation 12 is reduced to:

$$\begin{bmatrix} P' & U \\ Q & R \end{bmatrix} \begin{bmatrix} \underline{\delta} \\ \underline{s} \end{bmatrix} = p_e \begin{bmatrix} \underline{0} \\ -\underline{\hat{\tau}_e} \end{bmatrix}, \text{— (14)}$$

By solving Equation 14 with Equation 13 for ($\underline{\delta}$, $\underline{s}$), we can determine the motion of trapdoor faulting generated by pre-seismic magma overpressure p_e. Also, we can estimate the co-seismic changes of magma pressure and crack volume due to trapdoor faulting by substituting $\underline{\delta}$ into Equation 10, and the stress drop by substituting $\underline{s}$ into Equation 7.

4.2 Model setting

The source geometry employed for main results is shown in Figure 2. A partial ring fault is along an ellipse with a size of 3.6 km × 2.6 km on seafloor; the center is at (141.228°E, 25.4575°N), and its major axis is oriented N60°E. The fault is on the NW side of Kita-Ioto caldera with an arc length of 90° and dips inwardly with a dip angle of 83°; this fault setting on the NW side is based on our moment tensor analysis that suggests a ring fault orientated in the NE–SW direction (see Text S1, for details). The fault's down-dip end connects to a horizontal crack at a depth of 2 km. The crack is elliptical in shape, 15 % larger than the size of an ellipse traced along the fault's down-dip end. After discretizing the source geometry into sub-faults and sub-cracks, the four interaction matrices (*P*, *Q*, *R*, and *U*) between sub-faults and sub-cracks are computed by the triangular dislocation (TD) method (Nikkhoo & Walter, 2015), when we assume the Poisson's ratio of 0.25 and the Lame's constants λ and μ of 5 GPa.

The product $V_0\beta_m$ controls how the magma-filled crack responds to stress perturbation by faulting, as explained by Zheng et al. (2022). For main results, we assume the crack volume V_0 and the magma compressibility β_m as 1.5 x 10^{10} m^3 (corresponding to a crack thickness of ~500 m) and 1.0 x 10^{-10} Pa^{-1} (from a typical value for degassed basaltic magma [e.g., Kilbride et al., 2016]), respectively, thereby, $V_0\beta_m$ = 1.5 m^3/Pa. This product value is similar to Zheng et al.'s (2022) estimates for a magma reservoir of Sierra Negra caldera.

We emphasize that the model setting above, which is used to obtain main results shown in Section 5, is just an assumption. The location of the ring fault cannot be constrained from the earthquake information of the GCMT catalog, since the solutions can contain horizontal location errors up to ~40 km (Hjörleifsdóttir & Ekström, 2010; Pritchard et al., 2006). The bathymetry data containing several cones found on the NW side of the caldera floor (Figure 1c) may suggest an existence of a fault system, given such structures often formed over a sub-caldera ring fault (e.g., Cole et al., 2005), but this is not decisive information. Also, we have no constraint on the magma compressibility and the reservoir depth. In Section 6.1, we will test the sensitivity to those possible uncertainties in model setting.

4.3 Constraint from the tsunami data of the 2008 Kita-Ioto caldera earthquake

We apply the mechanical model of trapdoor faulting to the tsunami data of the 2008 Kita-Ioto caldera earthquake. Utilizing the linear relationship between ($\underline{\delta}$, $\underline{s}$) and p_e through Equation 14, we estimate the pre-seismic magma overpressure p_e causing the earthquake by constraining the magnitude of trapdoor faulting from the tsunami data.

For estimation of p_e, we prepare a model of trapdoor faulting due to unit pre-seismic magma overpressure p_e = 1 Pa, which we call unit-overpressure model, and then simulate a tsunami OBP waveform at the station 52404 from the model (see the methodology in Section 4.4). We denote the synthetic waveform as $\underline{\widehat{m}}$ and consider it as the tsunami OBP amplitude due to unit overpressure, whose unit is [mm H_2O/Pa]. Because of the linearity of the tsunami propagation problem we employ, the amplitude of tsunami waveform is linearly related to the magnitude of trapdoor faulting, and thereby to the pre-seismic magma overpressure p_e through Equation 14. Therefore, the synthetic tsunami waveform from trapdoor faulting due to an arbitrary p_e can be expressed as $\underline{m} = p_e \underline{\widehat{m}}$. Supposing that the tsunami signal from the 2008 earthquake recorded in the OBP data (denoted by $\underline{d}$) is reproduced well by $\underline{m}$, we can estimate the pre-seismic magma overpressure p_e from:

$$p_e = \frac{\rho_d}{\hat{\rho}}, \text{— (15)}$$

where ρ_d and $\hat{\rho}$ are the root-mean-square (RMS) amplitudes of $\underline{d}$ and $\underline{\widehat{m}}$ (in units of [mm H_2O] and [mm H_2O/Pa]), respectively. The time window for calculating the RMS amplitudes is set as it includes major oscillations in earlier parts of the observed waveform (see the gray line in Figure 1d).

4.4 Tsunami waveform simulation

A tsunami waveform from the unit-overpressure model $\underline{\hat{m}}$ is synthesized as follows. Assuming ($\underline{\delta}$, $\underline{s}$) of the unit-overpressure model, we compute the vertical seafloor displacement by the TD method, and convert it to vertical sea-surface displacement by applying the Kajiura filter (Kajiura, 1963). We then simulate the tsunami propagation over the time of 12,000 s from the sea-surface displacement over Kita-Ioto caldera, generated instantly at the earthquake origin time, by solving the linear Boussinesq equations (Peregrine, 1972) in the finite-difference scheme of the JAGURS code (Baba et al., 2015). The simulation is done with a two-layer nested bathymetric grid system, composed of a broad-region layer with a grid size of 18 arcsec (~555 m) derived from JTOPO30 data, and a caldera-vicinity-region layer with a grid size of 6 arcsec (~185 m), obtained by combining data from M7000 series and JTOPO30. The computation time step is 0.5 s, as the Courant-Friedrichs-Lewy (CFL) condition is satisfied. The outputted 2-D maps of sea-surface wave heights, every 5 s, are converted into maps of OBP perturbation by incorporating reduction of tsunami pressure perturbation with increasing water depth (e.g., Chikasada, 2019). The synthetic waveform of OBP perturbation at the station 52404 is obtained from the OBP maps.

The linear Boussinesq equations employed above do not include the effects of the elastic Earth, the seawater compressibility, and the gravitational potential change, and are less accurate for computation of higher-frequency waves due to the error of dispersion approximation (Sandanbata, Watada, et al., 2021). Hence, we apply a phase correction method for short-period tsunamis (Sandanbata, Watada, et al., 2021) to improve the synthetic waveform accuracy by incorporating the effects (i.e., elastic Earth, compressible seawater, and gravitation potential change) and by correcting the approximation error.

5 Results

5.1 Source model of the 2008 Kita-Ioto caldera earthquake

Under the model setting explained in Section 4.2 (Figure 2), we obtain a trapdoor faulting model for the 2008 Kita-Ioto caldera earthquake that explains the OBP tsunami data (Figure 3). The pre-seismic magma overpressure p_e constrained from the OBP tsunami data is 11.8 MPa. Figures 3b and 3c show the spatial distributions of the ring-fault slip $\underline{s}$ and the crack opening/closing $\underline{\delta}$ during trapdoor faulting. Large reverse slip at maximum of 8.9 m is on the ring fault, near which the inner crack opens by 5.5 m at maximum and the outer closes by 2.7 m. In the SE area, the crack closes broadly with a maximum value of 0.86 m. In total, the crack volume increases by ΔV = 0.0030 km^3. The co-seismic magma pressure change Δp is –1.97 MPa during trapdoor faulting, meaning that the magma overpressure drops by 16.7 % relative to the pre-seismic state and makes additional storage for magma. The response of the magmatic system to faulting may have postponed eruption timing; on the other hand, post-seismic magma overpressure is estimated to remain at a high level (~9.8 MPa) even after trapdoor faulting.

The obtained trapdoor faulting model is predicted to cause large asymmetric caldera-floor uplift, thereby generating a tsunami efficiently. The large seafloor displacement is concentrated near the fault, with the maximum uplift of as large as 5.6 m and outer subsidence of 2.8 m (Figure 3d). The sea surface displacement is smoothed by the low-pass effect of seawater, resulting in seawater uplift of 3.6 m within the caldera rim with the exterior subsidence of 1.1 m (Figure 3e). Figure 3f compares the synthetic tsunami waveform from the model with the OBP tsunami signal recorded at the station 52404, which demonstrates good waveform agreement, including later phases that are not used for the amplitude fitting. In addition, the spectrogram analysis confirms quite similar tsunami travel times and dispersive properties of the synthetic and observed waveforms (Figures 3g and 3h). These results support the reasonability of our mechanical model for the 2008 Kita-Ioto caldera earthquake.

5.2 Pre-seismic state just before trapdoor faulting

From the mechanical model, we consider how trapdoor faulting is caused by the inflated crack. In the pre-seismic state just before trapdoor faulting, the crack has inflated with vertical opening $\underline{\delta_e}$ of 12.1 m at maximum due to the pre-seismic magma overpressure p_e (Figure 4a). The inner volume has been increased by 0.21 km^3 relative to that in the reference state. This pre-seismic crack opening generates the shear stress on the fault $\underline{\tau_e}$, which takes its maximum value of 11.6 MPa (Figures 4b); this value corresponds to the stress drop during trapdoor faulting, because we assume that the stress totally vanishes co-seismically.

In a simple earthquake paradigm of the stick-slip motion, which assumes that slip occurs when the shear stress overcomes the static frictional stress (e.g., pp. 14 of Udias et al., 2014), the fault requires friction to remain stationarity until faulting occurrence. The total normal stress on the fault $\underline{\sigma_0^F}$ is the sum of the effects of the crack opening $\underline{\sigma_e^F}$ (Figure 4c) and the lithostatic and seawater loading $\underline{\sigma_{lit}^F} + \underline{\sigma_{sea}^F}$, as shown in Figure 4d (see the caption). By taking a ratio of the area-averaged values of $\underline{\tau_e}$ and $\underline{\sigma_e^F}$, the static friction coefficient on the ring fault can be estimated as 0.31. The frictional fault system may enable the caldera system to accommodate the high magma overpressure without fault slip until trapdoor faulting. Note that, however, sophisticated modeling approaches including realistic fault friction law will be needed for investigation of the dynamic initiation process.

5.3 Deformation and elastic stress change in the host rock

Our model demonstrates how trapdoor faulting deforms the host rock and changes its elastic stress. With the model outputs, we compute the displacement, stress and strain fields in the host rock along an SE–NW profile across the caldera (see the dashed line in Figure 3c) by the TD method; the pre-seismic state is from $\underline{\delta_e}$, the co-seismic change is from ($\underline{\delta}$, $\underline{s}$), and the post-seismic state is the sum of the pre-seismic state and the co-seismic change. We also calculate the shear-strain energy from the stress and strain fields (e.g., Saito et al., 2018). When we denote the stress tensors in the host rock as:

$$\tau_{ij} = \tau'_{ij} + \frac{1}{3}\tau_{kk}\delta_{ij}, \text{— (16)}$$

where τ'_{ij} is the deviatoric components, the shear-strain energy density W in the elastic medium can be expressed as:

$$W = \frac{1}{4\mu}\tau'_{ij}\tau'_{ij}. \text{— (17)}$$

Note that the shear-strain energy density is zero in the reference state ($p = p_0$), where the deviatoric stress is assumed to be zero. Using Equation 17, the shear-strain energy density in the pre- and post-seismic states, W^{pre} and W^{post}, can be calculated with the deviatoric shear stress. The co-seismic change in the shear-strain energy density is obtained by:

$$\Delta W = W^{post} - W^{pre}. \text{— (18)}$$

Figures 5a–5c show displacement in the host rock along the SE–NW profile. In the pre-seismic state (Figure 5a), since the fault accommodates no slip, the host rock deforms purely elastically from the reference state due to the opening crack and causes large uplift of the caldera surface by 8.8 m at maximum at the caldera center. During trapdoor faulting, the co-seismic displacement is concentrated along the fault (Figure 5b). The inner caldera block uplifts by 5.7 m at maximum, while the outer host rock moves downward by 3.2 m. The fault motion accompanies crack opening beneath the NW side of the caldera block, whereas slight downward motion is seen in the SE part of the caldera block, which can be attributed to elastic response to magma depressurization. Figure 5c shows the displacement in the post-seismic state, where the upward displacement is confined within the caldera block, with cumulative uplift of 9.9 m at maximum, from the center to near the fault, while notable deformation is not found outside the fault. As shown in Figure 5d, the pre-seismic seafloor displacement takes its uplift peak in the center, while after trapdoor faulting the seafloor becomes almost flat on the NW side near the fault. This indicates that if we take a long term including the pre-seismic inflation and trapdoor faulting, the caldera causes a block-like motion with a clear boundary cut by the fault.

In terms of the stress and the shear-strain energy, trapdoor faulting can be considered as a process that releases the shear-strain energy accumulated in the host rock. Figures 5e–5g show the shear-strain energy density with the principal axes of the stress field in the host rock along the same SE–NW profile. In the pre-seismic state, the shear-strain energy density is concentrated around the crack edge, or near the fault (Figure 5e). The plunge of the maximum compressional stress near the fault ranges from ~50° in the middle of the fault, which preferably induces a reverse slip on a steeply dipping fault. During trapdoor faulting (Figure 5f), the shear-strain energy density near the fault on the NW side dramatically decreases. Eventually, in the post-seismic state (Figure 5g), the shear-strain energy density almost vanishes near the fault. Note that, on the other hand, the shear-strain density is only slightly reduced on the SE side in response to co-seismic magma depressurization and remains high even after trapdoor faulting. We speculate that the remaining shear-strain energy may be released by other causes, such as aseismic fault slip, a subsequent trapdoor faulting, or viscoelastic deformation of the host rock, which are not incorporated in our modeling; we will discuss the limitations of our models in Section 6.5.

6 Discussion

6.1 Model uncertainties

Our source model has been constructed in the model setting as described in Section 4.2. However, since a single tsunami waveform data at a distant location has low sensitivity to the source details, we do not have enough data to constrain the sub-surface structure and magma property. Hence, our model outputs vary depending on how the model setting is assumed priorly.

6.1.1 Depth of a horizontal crack

The depth of a horizontal crack, or a magma reservoir, significantly influences our pre-seismic magma overpressure estimation. When a deeper crack is assumed at a depth of 4 km below seafloor (Figure 6), the estimated magma overpressure p_e is 22.26 MPa, almost a factor of two larger compared to our main result assuming a depth of 2 km (Figure 3). The obtained model with a 4-km deep crack explains the tsunami data well, even better than that with a 2-km deep crack (compare waveforms and spectrograms in Figures 3f–3h and 6f–6h), implying preference of the deeper crack model. When a crack is located deeper in the crust, the magnitude of the crack opening per unit magma overpressure becomes smaller because it is farther from the free-surface seafloor (Fukao et al., 2018). This lowers the shear stress on the fault generated per unit magma overpressure, and thereby larger pre-seismic magma overpressure is required to cause a similar-sized earthquake and tsunami. Despite the large difference in pre-seismic magma overpressure, the estimated co-seismic parameters for the 2008 earthquake, such as magnitudes of fault slips, crack deformation, and changes in magma pressure and crack volume, do not change largely.

6.1.2 Arc length of a ring fault

The arc length of a ring fault is also an important factor affecting our modeling. As shown in Figure 7, when we assume a ring fault with an arc length of 180°, or a half-ring fault, on the NW side, pre-seismic magma overpressure p_e is estimated as 4.84 MPa, less than half of the value from our main results assuming an arc length of 90° (Figure 3). This large difference can be attributed to two main causes. First, the average fault slip amount is known to be proportional to the faut length when the stress drop is identical (Eshelby, 1957); therefore, a longer ring fault causes large slip efficiently, compared to that on a shorter arc length.

Additionally, trapdoor faulting with a longer fault uplifts larger volume of seawater over a broader area (compare Figures 7e and 3e), making its tsunami generation efficiency higher.

Although smaller magma overpressure (p_e = 4.84 MPa) is estimated in the case with a ring-fault arc angle of 180°, we emphasize that the co-seismic magma pressure change Δp is as large as –1.99 MPa. The magma overpressure efficiently drops by 41.1 % from the pre-seismic state, in contrast to the ratio of only 16.7 % in the case of an arc length of 90° (see Section 5.1). The difference arises from the fact that the fault slip along a longer segment induces the crack opening in a broader area and increases the inner volume more, resulting in more efficient pressure relief. The two models with different ring-fault arc lengths produce very similar tsunami waveforms at the station 52404 (compare Figures 7f and 3f), indicating the difficulty in distinguishing the arc length from our dataset. However, these results provide an important insight that the magma pressure drop ratio strongly depends on a fault length ruptured during trapdoor faulting, suggesting importance to investigate the intra-caldera fault geometry for robust quantification of magma pressure change due to faulting.

6.1.3 Other uncertainties

We discuss on effects of the product $V_0\beta_m$, which controls how the magma-filled crack responds to stress perturbation by faulting. The effects in extreme cases are discussed by Zheng et al. (2022); when $V_0\beta_m \to 0$, the crack involves no total volume change ($\Delta V \to 0$), while a magnitude of magma pressure drop becomes the largest; on the other hand, when $V_0\beta_m \to \infty$, the net volume change of the crack is at maximum, while no pressure change occurs ($\Delta p \to 0$). In previous studies of the 2018 Kilauea caldera collapse and eruption sequence, the estimated product ranges 1.3–5.5 m^3/Pa (Anderson et al., 2019; Segall & Anderson, 2021). We assumed $V_0\beta_m$ = 1.5 m^3/Pa for our main results, which is close to the lower end of the range. To examine the model variations, we try the source modeling alternatively by assuming $V_0\beta_m$ = 6.0 m^3/Pa, near the upper limit of the range estimated in the case of Kilauea. For the larger $V_0\beta_m$, the area of the crack opening becomes broader, while a magnitude of the closure on the other side becomes smaller (Figures S4a–S4c; compare them with Figures 3a–3c). The sea-surface displacement is thereby broader (Figure S4e), exciting long-period tsunamis more efficiently that arrives as earlier waveform phases used for the amplitude fitting (Figure S4f). Thus, in this case, our estimation of the pre-seismic magma overpressure, p_e = 9.11 MPa, becomes slightly smaller than the main result (p_e = 11.8 MPa); on the other hand, we estimate smaller magma pressure drop (Δp = −1.27 MPa) and a larger crack volume increase (ΔV = 0.0076 km^3). These suggest that if we take a plausible range of $V_0\beta_m$, variations of our estimations are insignificant.

It is uncertain on which side of the caldera the ruptured fault is located. Based on our moment tensor analysis (Text S1), the fault ruptured during the 2008 earthquake can be estimated to be oriented manly in the NE–SW direction, allowing us to assume two different fault locations, either of the NW or SE sides of the caldera; for our main results, we chose the model with a fault on the NW side. Here, we alternatively assume a fault on the SE side to obtain another source model, and consequently estimate the pre-seismic magma overpressure p_e as 15.36 MPa (Figure S5). Despite the fault location difference, the tsunami data is explained well by the model with a SE-sided fault (Figure S5f). The change of the estimated magma overpressure can be attributed to effects of tsunami directivity and complex bathymetry in the source region on the wave amplitude of a tsunami arriving at the station. Thus, our limited dataset is not sufficient to determine well the fault location, but the uncertainty in fault location influences our estimations insignificantly.

6.2 Comparison with previous studies

Our quantification of pre-seismic magma overpressure before trapdoor faulting in Kita-Ioto caldera (p_e = 4–22 MPa) is of the same order of magnitude as those estimated geodetically for the subaerial caldera of Sierra Negra. Gregg et al. (2018) applied a thermomechanical finite element method (FEM) model to long-term geodetic data and estimated that magma overpressure of ~10 MPa in the sill-like reservoir induced a trapdoor faulting event that occurred ~3 hours before the eruption starting on 22 October 2005. Another trapdoor faulting event on 25 June 2018 (M_w 5.4) also preceded the 2018 eruption of Sierra Negra by ten hours; Gregg et al. (2022) employed the thermomechanical FEM approach to the long-term deformation and suggested that a similar magma overpressure <~15 MPa had been accumulated to cause the failure of the trapdoor fault system.

Zheng et al. (2022), on the other hand, quantified co-seismic magma pressure change by trapdoor faulting with an m_b 4.6 earthquake on 16 April 2005. By modeling the interaction between the intra-caldera fault system and the sill-like reservoir, Zheng et al. geodetically estimated the trapdoor faulting event with a maximum fault slip of 2.1 m reduced magma overpressure by 0.8 MPa; the slightly smaller pressure change, relative to our estimation ($|\Delta p| =$ 1–3 MPa) for the 2008 Kita-Ioto earthquake, may be explained by the discrepancies in the earthquake size or the length of a ruptured fault.

Sandanbata et al. (2023) compiled the seismic magnitude and the maximum fault slip of trapdoor faulting events and demonstrated their atypical earthquake scaling relationship; in other words, trapdoor faulting accompanies larger fault slip by an order of magnitude than those for similar-sized tectonic earthquakes. Source models presented in this study for the 2008 Kita-Ioto caldera earthquake also accommodate large fault slip ranging 5–10 m at maximum, which are clearly larger than those empirically predicted for M_W 5.3 tectonic earthquakes; for example, the empirical maximum slip for M_w 5.3 earthquake is only ~0.1 m, following Wells & Coppersmith (1994). This indicates the efficiency of intra-caldera fault systems in causing large slip, possibly due to their interaction with magma reservoirs and shallow source depth (Sandanbata et al., 2022).

6.3 Long-period seismic waveforms

For validation from a different perspective, we consider long-period seismic excitation by the mechanical source model that we have obtained based on the tsunami data. For this analysis, we follow the methodology used in Sandanbata et al. (2022; 2023), as the detailed procedures are described in Text S2. We here briefly summarize the method. We first approximate the trapdoor faulting model (Figure 3a) as a point-source moment tensor $\boldsymbol{M}_T$ by summing up partial moment tensors of the ring fault $\boldsymbol{M}_F$ and the horizontal crack $\boldsymbol{M}_C$ (Figure 8a–8c). We then compute long-period (80–200 s) seismic waveforms from the moment tensor $\boldsymbol{M}_T$ by using the W-phase package (Duputel et al., 2012; Hayes et al., 2009; Kanamori & Rivera, 2008) and compare the synthetic waveforms with broad-band seismic data from F-net and global seismic networks. In Figures 8d and S6, we show synthetic seismic waveforms from the moment tensor (Figure 8a), which reproduce well the observed seismograms. This supports that our trapdoor faulting model is plausible in terms of seismic excitation, as well as tsunami generation.

We note that the theoretical moment tensor obtained from our model (Figure 8a) is different from the GCMT solution; our theoretical solution has a seismic magnitude (M_w 5.6) and is characterized by large double-couple and isotropic components, while the GCMT solution is with a smaller magnitude M_w 5.3 and a dominant vertical-T CLVD component (Figure 1c). The difference can be explained by very inefficient excitation of long-period seismic waves by specific types of shallow earthquake sources (Fukao et al., 2018; Sandanbata, Kanamori, et al., 2021). As demonstrated in Figure S7, major parts of the long-period seismic waves of the trapdoor faulting model arise from limited moment tensor components that constitute a vertical-T CLVD moment tensor, equivalent to M_w 5.2 (Figure S7b), whereas the contribution by the horizontal crack $\boldsymbol{M_T}$, and $M_{r\theta}$ and $M_{r\phi}$ components in $\boldsymbol{M_F}$ are negligibly small. Hence, the GCMT solution determined with the long-period seismic waveforms becomes a vertical-T CLVD moment tensor with a smaller magnitude than that of the theoretical moment tensor of our model. The gap between theoretical and observed moment tensors of trapdoor faulting is discussed in more detail by Sandanbata et al. (2022).

6.4 Tsunami generation by other Kita-Ioto caldera earthquakes

We have conducted a survey of OBP data from the station 52404 to determine if there were any tsunami signals following the other Kita-Ioto caldera earthquakes (Figure S1), apart from that in 2008. Available data was found only for the event on 15 December 2015 (Figure 9a), for which a clear tsunami signal was recorded in the OBP data with a 15-s sampling interval (Figure 9b). On the other hand, we were unable to obtain OBP data to confirm tsunami signals from the earthquakes in 1992, 2010, 2017, and 2019. The station 52404 had not been deployed yet as of the 1992 event. For the other events, the bottom pressure recorders have been lost, preventing our access to its 15-s sampling-interval data. Although low-sampling data (15-min interval) sent via a satellite transfer are available, they are not useful for confirming tsunami signals with dominant periods of 100–500 s.

We further investigate the tsunami signal from the 2015 earthquake in comparison with that from the 2008 event. Note that the station location (20.7722N°, 132.3375E°) as of 2008 had shifted about 20 km northward to a new location (20.9478N°, 132.3122E°) as of 2015. To examine the similarity between the two earthquake events, we simulate a tsunami waveform at the station location as of the 2015 event from a model similar to that of the 2008 event. We assume the model setting with a deeper crack at a depth of 4 km, based on that presented in Section 6.1.1 (Figure 7). Since the GCMT catalog reports a smaller seismic moment for the 2015 event (M_0^{2015} = 8.1 × 10^{17} Nm) than that for the 2008 event (M_0^{2008} = 1.1 × 10^{18} Nm), we adjust the source model assuming a smaller pre-seismic overpressure of p_e = 16.41 MPa (= 22.26 MPa $\times \frac{M_0^{2015}}{M_0^{2008}}$).

Although the observed tsunami waveforms from the two earthquakes look different (compare the waveforms in Figures 7f and 9b), the trapdoor faulting model, based on the tsunami data form the 2008 earthquake, also explains that from the 2015 earthquake overall (Figure 9), simply by changing the station location. The nonnegligible waveform difference at the two nearby locations can be attributed to the focusing/defocusing effect by complex bathymetry along the path (Figure S8; see the figure caption for details). This suggests that the 2015 earthquake was caused by trapdoor faulting, in a similar way to the 2008 earthquake. The similarity is further supported by our moment tensor analysis (see Text S1). Thus, we confirmed tsunami signals from both of the two events. Therefore, we propose that the quasi-regularly repeating earthquakes with similar magnitudes and vertical-CLVD characters reflect the recurrence of trapdoor faulting in Kita-Ioto caldera, as observed in the three calderas of Sierra Negra, Sumisu, and Curtis, where trapdoor faulting events have recurred (Bell et al., 2021; Jónsson, 2009; Sandanbata et al., 2022, 2023).

6.5 Limitations of our mechanical trapdoor faulting model

Our mechanical model of trapdoor faulting has been developed under some simplifications to focus on the essential mechanics. In this subsection we discuss some factors simplified or ignored in our model, which may influence our results.

6.5.1. Stress drop ratio

The stress drop ratio during earthquakes has been controversial in general. Some studies reported complete or near-complete stress drop during tectonic earthquakes (Hasegawa et al., 2011; Ross et al., 2017), while the stress drop ratio can be partial and vary from earthquake to earthquake (Hardebeck & Okada, 2018). For intra-caldera earthquakes, several recent studies estimated stress drop during caldera collapses (Moyer et al., 2020; T. A. Wang et al., 2022), but our knowledge on the stress drop ratio in calderas is poor and the ratio may vary from caldera to caldera.

We have avoided the problem by simply assuming the complete stress drop as an extreme case (Equation 14, obtained by assuming α = 1 in Equation 12); this assumption can influence our estimation of the pre-seismic magma overpressure p_e. Because $\underline{s}$ and $\underline{\delta}$ are determined by the stress drop on the fault, not directly by pre-seismic magma overpressure (Equation 3), if a partial stress drop ratio α $(0 < \alpha < 1)$ is instead assumed in Equation 12, the trapdoor faulting size due to the same pre-seismic magma overpressure becomes smaller proportionally to α, and the tsunami amplitude does. In this case, larger magma overpressure by a factor of $1/\alpha$ is required to explain the observed tsunami amplitude. Hence, the complete stress drop assumption provides lower-limit estimation of pre-seismic magma overpressure in the model setting. On the other hand, estimations of co-seismic parameters, such as fault slip $\underline{s}$ and crack opening $\underline{\delta}$, and changes of magma pressure Δp and crack volume ΔV, do not change regardless of our assumption of the stress drop ratio α, since they are constrained form the tsunami amplitude.

6.5.2. Pre-slips and earthquake cycles

We have attributed the shear stress that generates trapdoor faulting to an inflating crack alone and neglected other factors that may also cause the stress on the fault. First, different segments of the intra-caldera ring fault may have caused microseismic or aseismic slips prior to the occurrence of M_w~5 trapdoor faulting. In Sierra Negra caldera, high microseismicity was observed along the western segment of the intra-caldera fault, leading to trapdoor faulting on the southern segment before eruption (Bell et al., 2021; Shreve & Delgado, 2023). Similarly, during the 2018 eruption and summit caldera collapse sequence of Kilauea, large collapse events accompanying M_w~5 earthquakes were located on the southeastern and northwestern sides of the summit caldera, while high microseismicity was found on other segments (Lai et al., 2021; Shelly & Thelen, 2019). T. A. Wang et al. (2023) further suggested non-negligible effects on large collapses of Kilauea by intra-caldera fault creep in the inter-collapse period. Such high microseismicity or creeping on other fault segments, in adjacent to the ruptured segment of trapdoor faulting, may impose additional shear stress.

Additionally, the recurrency of trapdoor faulting can play an important role in the stress accumulation on the fault. Similar earthquakes have been repeated near Kita-Ioto caldera (Figure S1), strongly suggesting recurrence of trapdoor faulting, as supported by the tsunami signal from the 2015 earthquake (see Section 6.4). If a similar earthquake repeated on the same segment of the fault and the stress drop is only partial, the remaining stress may influence subsequent trapdoor faulting events. Also, assuming that the earthquakes occur on different segments of the ring fault, an event on a segment increases the shear stress on its adjacent segment. Thus, in the presence of additional shear stress by pre-slips or creeping on different segments or previous trapdoor faulting events, the ring fault may be ruptured by smaller pre-seismic magma overpressure. For better understanding of the physics of trapdoor faulting, further studies of the earthquake cycle in calderas are crucial.

6.5.3. Other factors

Other factors simplified in our model, such as magma reservoir geometry, and viscoelasticity and heterogeneous rheological property of the host rock, may influence the mechanics of trapdoor faulting. While we have modeled a magma reservoir simply as an infinitely thin crack that lies horizontally, the reservoir should have a finite thickness and the geometry may not be flat, as estimated for that beneath Sierra Negra caldera (Gregg et al., 2022). The host rock has been also simplified as a homogeneous elastic medium, but the viscoelastic effects and thermal dependency of the rheological property may impact the deformation and stress and strain states in hot volcanic environments. For example, Newman et al. (2006) showed that the viscoelastic effect significantly reduces the estimated magma overpressure using surface deformation data at Long Valley caldera, compared to that based on a purely elastic model. The viscoelastic effect can be more important in the stress accumulation process, particularly during a long-term caldera inflation phase. Additionally, the temperature-dependency of the host-rock rheology is shown to have an impact on the stress accumulation process in the host rock, impacting on estimation of the timing of host-rock failures and eruption (Cabaniss et al., 2020; Zhan & Gregg, 2019). For further studies, it would be critical to incorporate these effects on the deformation and the stress-strain accumulation in the host rock, as done by previous studies employing the FEM modelling approach (e.g., Gregg et al., 2012; Le Mével et al., 2016; Zhan & Gregg, 2019).

7 Conclusions

We have presented a new mechanical model of trapdoor faulting that quantitatively links pre-seismic magma overpressure in a sill-like reservoir and the size of trapdoor faulting. We applied this model to a tsunami-generating submarine earthquake in 2008 around Kita-Ioto caldera, for quantifying the caldera's mechanical states. Our trapdoor faulting model explains well the tsunami signal recorded by a single distant ocean bottom pressure gauge, as well as regional long-period seismic waveforms. Although we acknowledge that other possible mechanisms (e.g., fluid-flow or volumetric-change source in magma reservoir) are not tested in this study, and that there is no direct observation of an active fault system in the caldera, our results suggest the plausibility of our hypothesis of the submarine trapdoor faulting in Kita-Ioto caldera. This is also supported by the similarity to trapdoor faulting events found recently in better-investigated submarine calderas (Sumisu and Curtis calderas). Repeating vertical-T CLVD earthquakes and another tsunami signal following the 2015 earthquake suggest the recurrence of trapdoor faulting in Kita-Ioto caldera.

Our mechanical models enable us to infer the pre-seismic magma overpressure beneath the submarine caldera, through quantification of the trapdoor faulting size. In an example case with a ring fault with an arc length of 90° and a horizontal crack at a depth of 2 km in the crust as the main model setting, we estimate that pre-seismic magma overpressure over ~10 MPa causes the trapdoor faulting event, and that the co-seismic magma pressure drops by ~15 %. Yet, since uncertainty on the source geometry remains due to our limited dataset, or a single tsunami record, these estimated values related to magma overpressure vary by a factor of half to twice, depending on model setting; the pre-seismic magma overpressure ranges approximately from 5 to 20 MPa, and the co-seismic overpressure drop ratio from 10 to 40 %. For example, a longer ring fault with an arc angle of 180° requires less magma overpressure to generate the similar-sized tsunami but more effectively reduces the overpressure; on the other hand, larger magma overpressure is estimated when the source has a crack at a deeper depth of 4 km. The significant variations suggest that magmatic systems beneath calderas can be strongly influenced by source properties of trapdoor faulting. Therefore, it is critical to study trapdoor faulting in active calderas and its source properties, which would help us obtain more robust estimation of magma overpressure or stress states, providing rare opportunity to achieve comprehensive understanding of how inflating calderas behave in the ocean.

Acknowledgments

We thank Rachel Abercrombie (Editor) and Associate Editor for handling our manuscript, and two anonymous reviewers for their constructive suggestions. We thank also Kurama Okubo for helpful discussion. This study is funded by the JSPS KAKENHI (Grant numbers JP20J01689).

Open Research

OBP data of DART system is available from DART® Bottom Pressure Recorder Data Inventory of National Oceanic and Atmospheric Administration (National Oceanic and Atmospheric Administration, 2005; https://www.ngdc.noaa.gov/hazard/dart/). Bathymetric data of M7000 Digital Bathymetric Chart and JTOPO30 are available from (Japan Hydrographic Association, 2011; 2022; https://www.jha.or.jp/shop/index.php?main_page=categories). F-net seismic data of F-net are available from the NIED (National Research Institute for Earth Science and Disaster Resilience, 2019; https://www.fnet.bosai.go.jp/top.php?LANG=en). Global seismic data were downloaded through the EarthScope Consortium Wilber 3 system (https://ds.iris.edu/wilber3/) or EarthScope Consortium Web Services (https://service.iris.edu/), including the following seismic networks: the IU and II (GSN; Albuquerque Seismological Laboratory/USGS, 2014; Scripps Institution of Oceanography, 1986), and the IC (New China Digital Seismograph Network: NCDSN; Albuquerque Seismological Laboratory (ASL)/USGS, 1992). The earthquake information is available from the GCMT catalog (Ekström et al., 2012; https://www.globalcmt.org/). The Geoware TTT software (Geoware, 2011; https://www.geoware-online.com/tsunami.html) is used for estimating tsunami arrival times. Focal mechanisms representing moment tensors are plotted with a MATLAB code of focalmech (Conder, 2019). The data of the source model proposed for main results in this study (Figure 3) can be obtained from an open-access repository of Zenodo (Sandanbata & Saito, 2023).

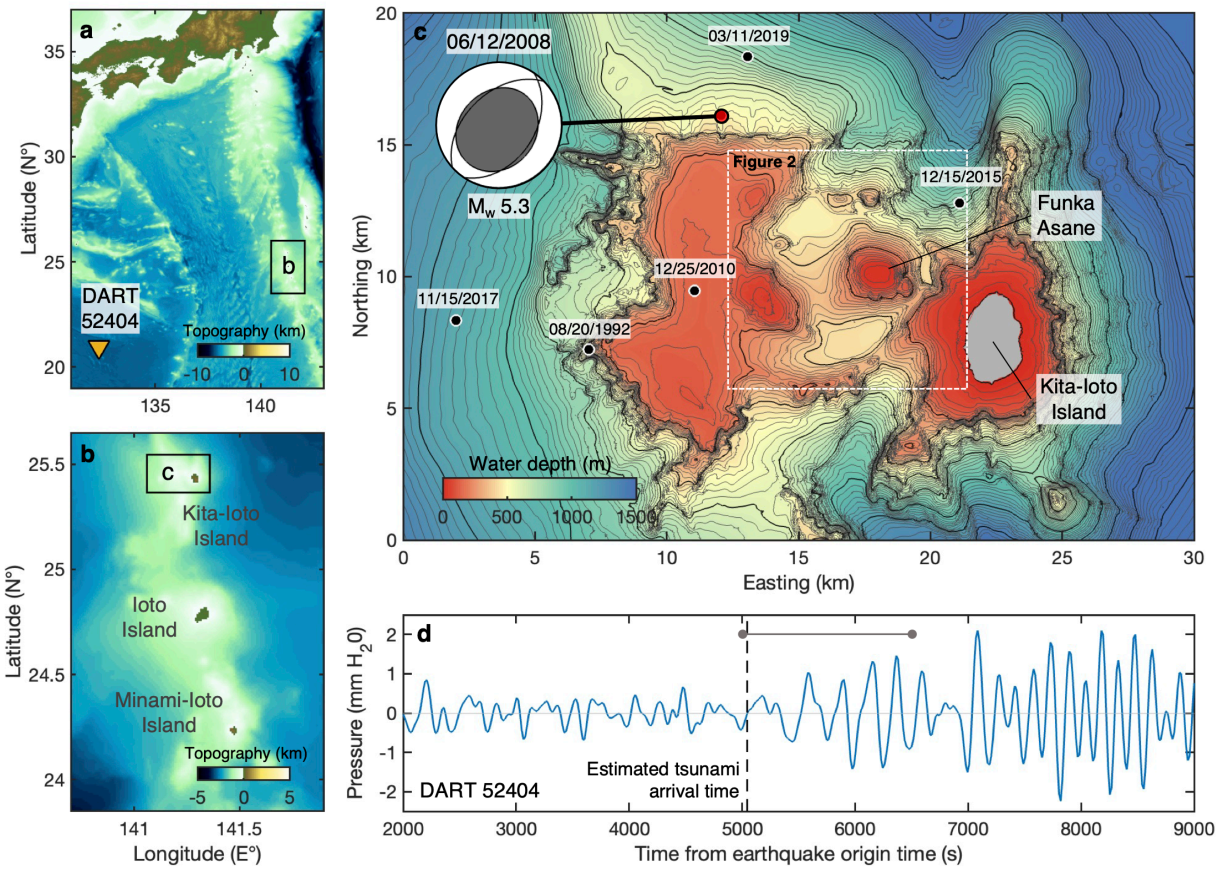

Figure 1. Vertical-T CLVD earthquakes near Kita-Ioto caldera. (**a**) Map of the southern ocean of Japan. Orange triangle represents the ocean-bottom-pressure (OBP) gauge of DART 52404. (**b**) Map of the region near Kita-Ioto Island. (**c**) Bathymetry of the region near Kita-Ioto caldera, a submarine caldera with a size of 12 km x 8 km, near Kita-Ioto Island. Funka Asane is the summit of a cone structure within the caldera rim. Red circle represents the location of the 2008 Kita-Ioto earthquake with its moment tensor, whereas black circles represent locations of similar events; the earthquake information is from the GCMT catalog (Ekström et al., 2012). The focal mechanism is shown as projections of the lower focal hemisphere, and the orientation of the best double-couple solution is shown by thin lines. (**d**) Tsunami waveform recorded at the OBP gauge of DART 52404. Dashed gray line represents the tsunami arrival time estimated using the Geoware TTT software (Geoware, 2011). Solid gray line represents the data length for calculating the root-mean-square (RMS) amplitudes (Equation 15). This waveform data is obtained by removing the tidal trend from and by applying the bandpass (2–10 mHz) Butterworth filter to the raw OBP data for 12,000 s after the earthquake origin time. Note that

oscillations of OBP changes with a few mm H_2O are recorded after the estimated arrival time, indicating tsunami signals.

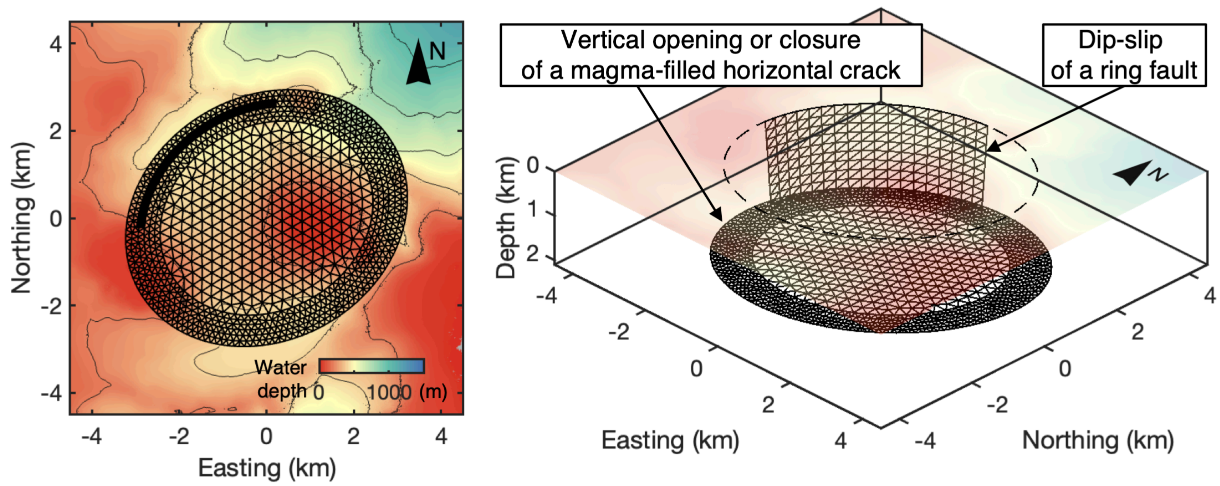

748

749 **Figure 2**. A source structure for the mechanical model of trapdoor faulting viewed from top

750 (left) and southeast (right). Gray lines are plotted every water depth of 200 m.

751

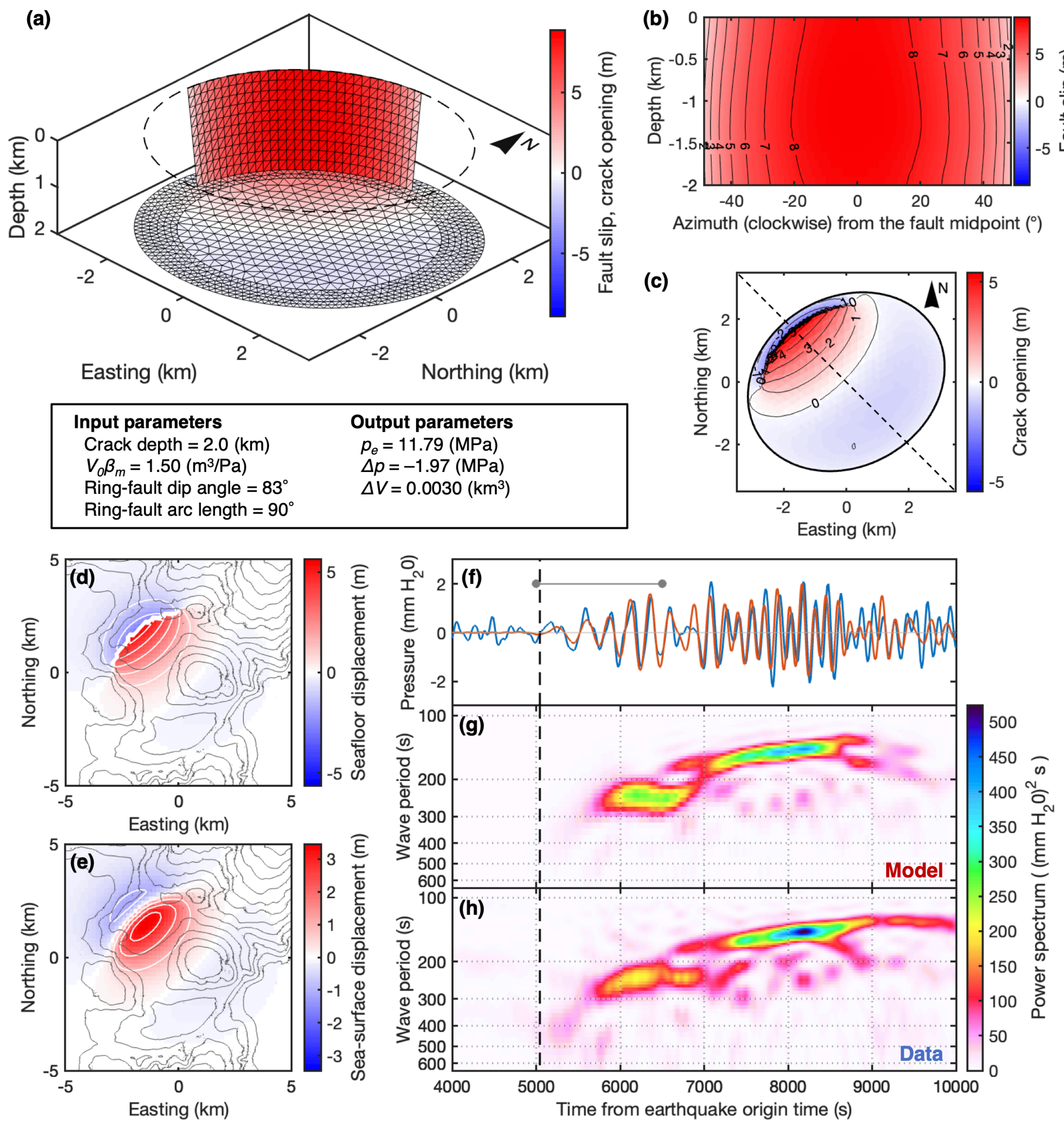

Figure 3. Mechanical trapdoor faulting model of the 2008 Kita-Ioto earthquake. (**a**) Mechanical model viewed from southeast, represented by dip slip of the ring fault $\underline{s}$ and vertical deformation of the crack $\underline{\delta}$. Red color on the ring fault represents reverse slip, while red and blue colors on the horizontal crack represent vertical opening and closure, respectively. (**b** and **c**) Spatial distributions of (**b**) the ring fault and (**c**) the horizontal crack. In **b**, the fault is viewed from the caldera center, and the azimuth from the caldera center to arbitrary point on the fault is measured clockwise from the midpoint of the fault. In **c**, dashed line represents a profile shown in Figure 5.

(**d** and **e**) Vertical displacement of seafloor (**d**) and sea surface (**e**) due to the model. Red and blue colors represent uplift and subsidence, respectively, with white lines plotted every 1.0 m. Black lines represent water depth every 100 m. (**f**) Comparison between a synthetic tsunami waveform from the model (red line) and the observed OBP waveform (blue line) at the station 52404. Solid gray line represents the data length for calculating the root-mean-square (RMS) amplitudes (Equation 15). (**g** and **h**) Spectrograms of the (**g**) synthetic and (**h**) observed waveforms. In **f**–**h**, black dashed line represents the tsunami arrival time.

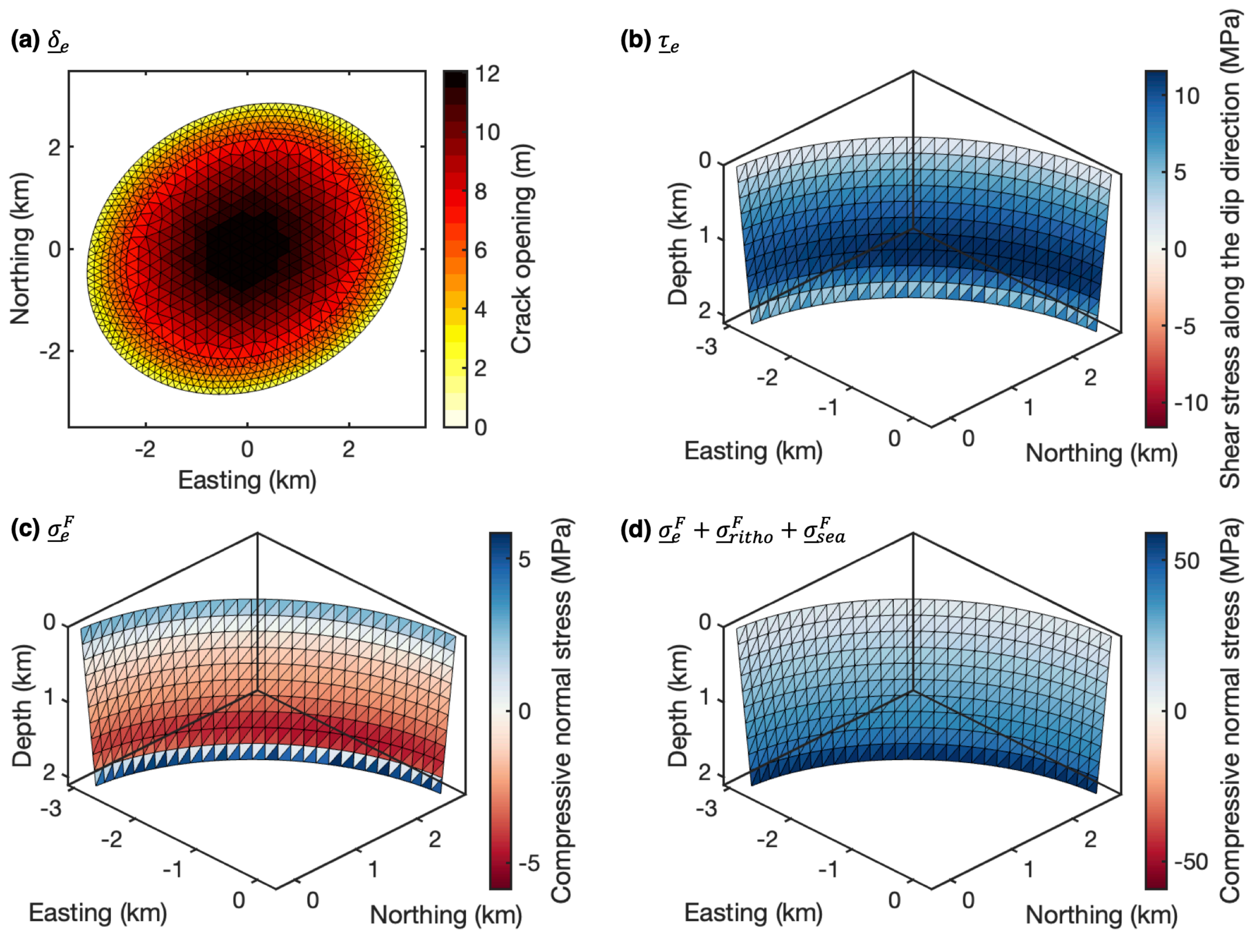

Figure 4. Pre-seismic state of the fault-crack system just before trapdoor faulting. (**a**) Distribution of the crack opening, $\underline{\delta_e}$. (**b**) Critical shear stress along dip-slip direction on the ring fault, $\underline{\tau_e}$. (**c**) Normal stress on the ring fault induced by the critically opening crack, $\underline{\sigma_e^F}$. In **b** and **c**, blue and red colors represent compressive and extensional normal stress, respectively. (**d**) Total normal stress on the ring fault, $\sigma_0^F = \sigma_e^F + \sigma_{lit}^F + \sigma_{sea}^F$; here, $\sigma_{lit}^F = \rho_h z g$, where ρ_h, z, and g are the host rock density (2,600 kg/m^3), the depth of each mesh, and the gravitational acceleration (9.81 m/s^2), respectively, and $\sigma_{sea}^F = \rho_s H g$, where ρ_s and H are the seawater density and the approximated thickness of the overlying seawater layer (1,020 kg/m^3 and 400 m), respectively.

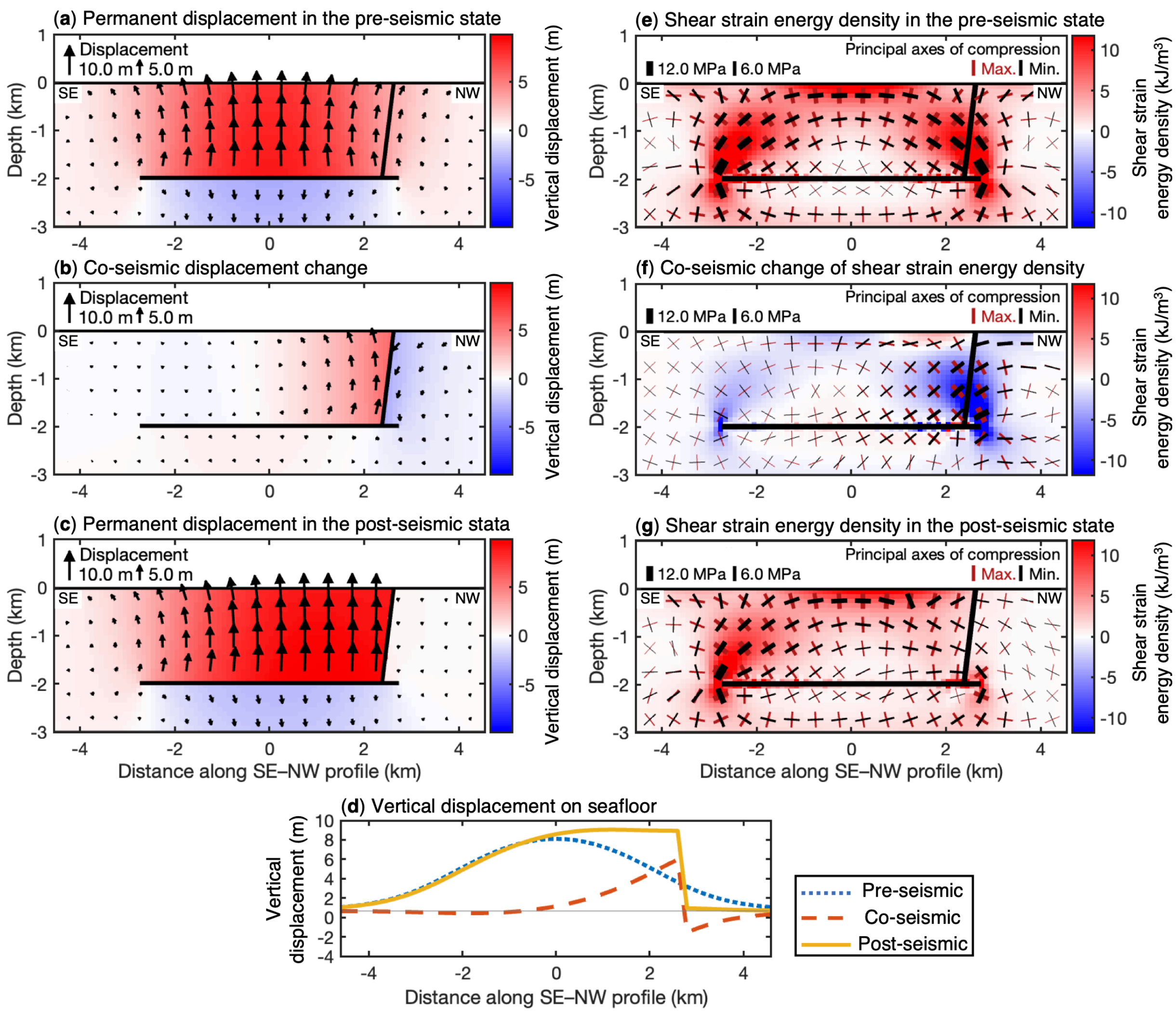

Figure 5. Displacement and shear-strain energy density in the host rock, along a SE–NW profile shown in Figure 3c. (**a**–**c**) Displacement, relative to the reference state ($p = p_0$): (**a**) the pre-seismic state just before trapdoor faulting, (**b**) the co-seismic change due to trapdoor faulting, and (**c**) the post-seismic state after trapdoor faulting. (**d**) Vertical seafloor displacement in each state shown in **a**, **b**, and **c**. (**e**–**g**) Shear-strain energy density W: (**e**) the pre-seismic state, (**f**) the co-seismic change, and (**g**) the post-seismic state. Color represents shear-strain energy density, and bars represent principal axes of compression projected on the profile, whose thickness reflects half the differential stress change $(\sigma_1 - \sigma_3)/2$, where σ_1 and σ_3 are the maximum and minimum stress, respectively.

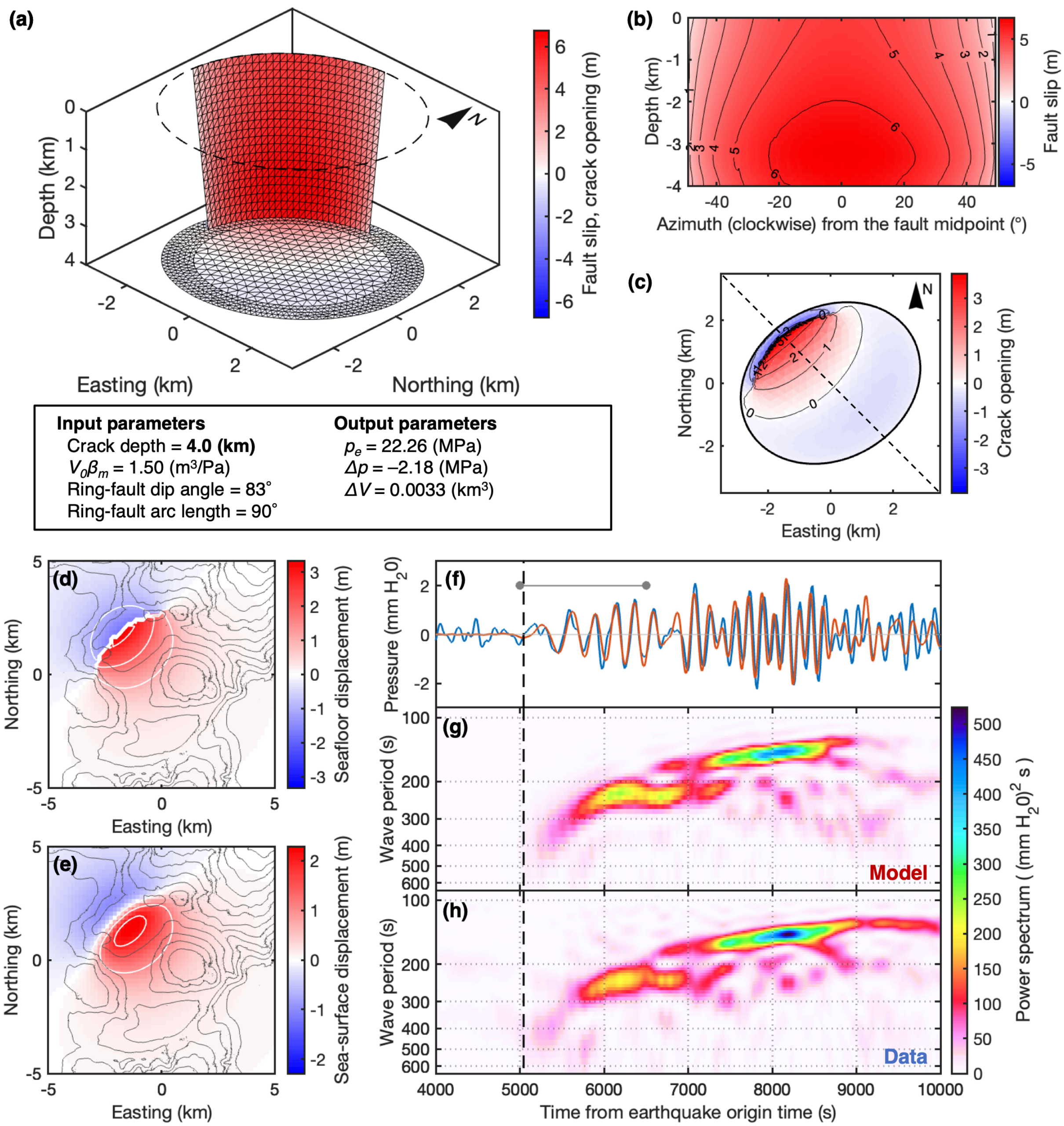

Figure 6. Same as Figure 3, but for a model with a horizontal crack at a depth of 4 km. See details in Section 6.1.1.

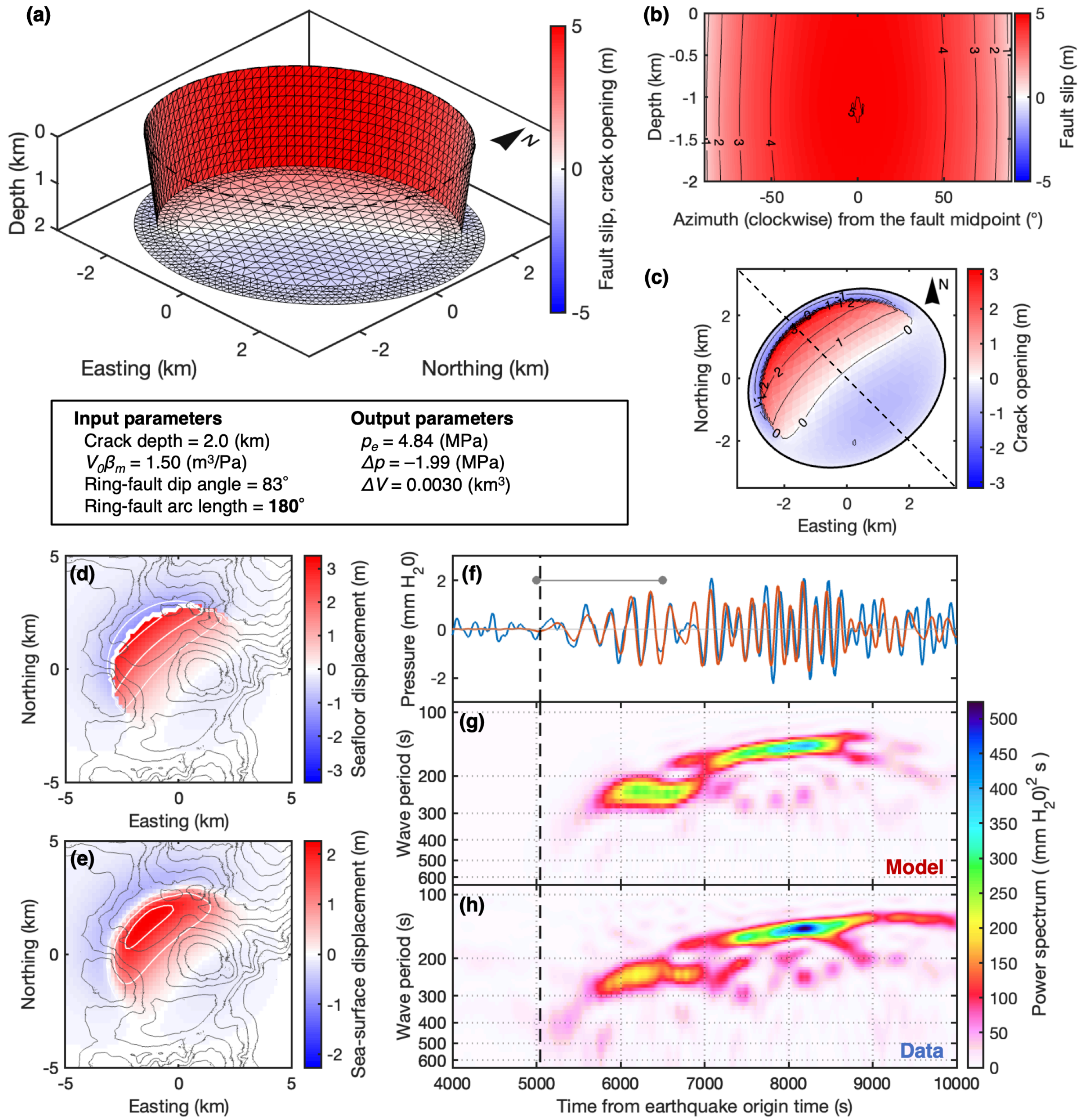

793

794 **Figure 7**. Same as Figure 3, but for a model with a longer ring fault of an arc ancle of 180°. See

795 details in Section 6.1.2.

796

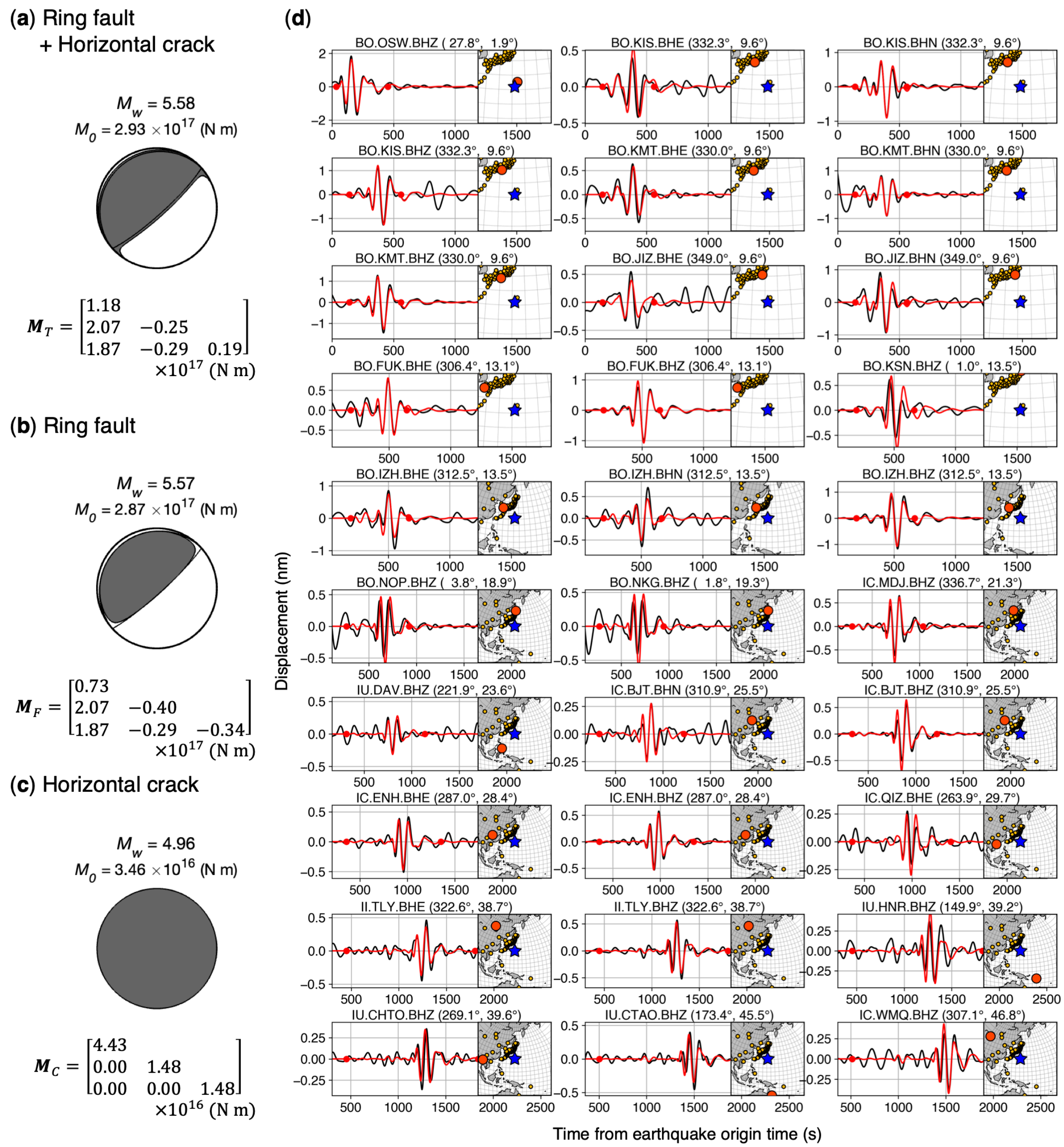

Figure 8. Long-period (80–200 s) seismic waveform modeling. (**a**) Moment tensor of the model, composed of partial moment tensors of (**b**) the ring fault and (**c**) the horizontal crack. (**d**) Comparison between synthetic waveforms (red line) and the observation (black line) at representative stations. In inset figures, a large red circle and a blue star represent the station and the earthquake centroid, respectively. On the top of each panel, the network name, station name, record component, station azimuth, and epicentral distance are shown. Note that waveform comparisons in all the tested seismic records are shown in Figure S6.

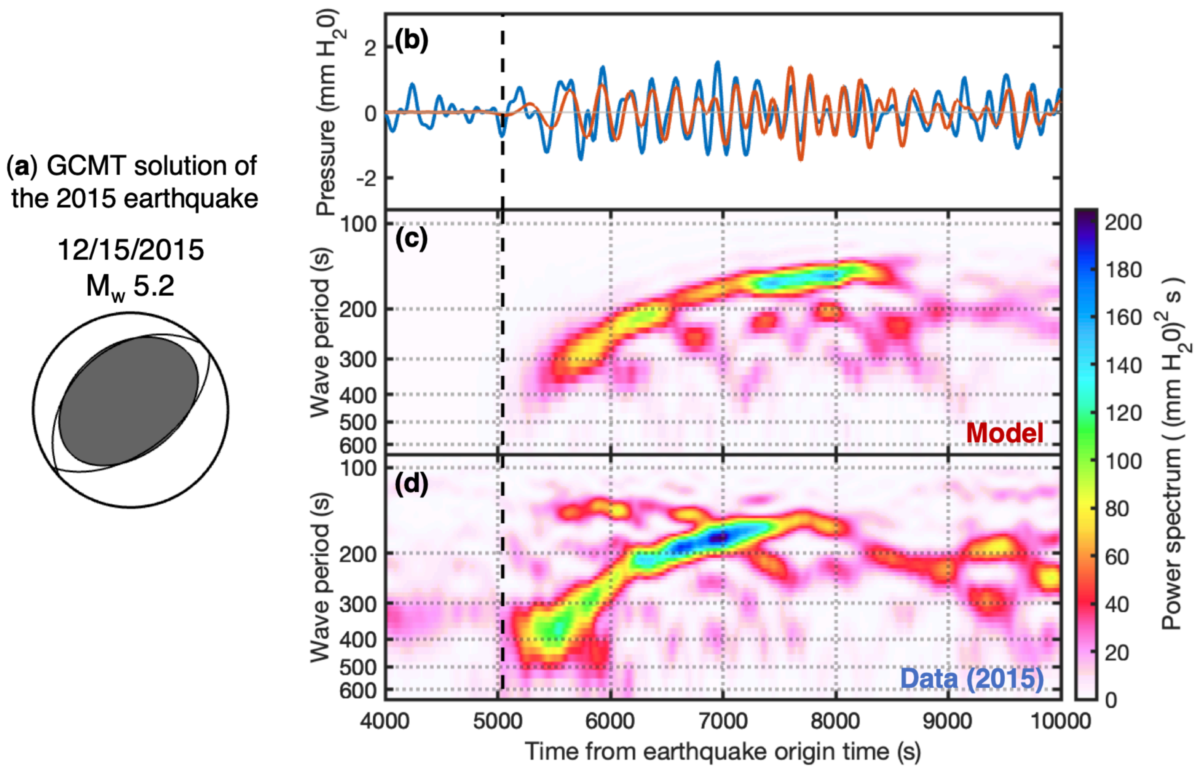

Figure 9. Tsunami waveform data from the 2015 earthquake. (**a**) The GCMT solution of the Kita-Ioto caldera earthquake on December 15, 2015. (**b**) Comparison between a synthetic tsunami waveform from a source model adjusted from the 2008 earthquake model (red line; see Section 6.4) and the observed OBP waveform (blue line) at the station 52404. (**c**–**d**) Spectrograms of the synthetic waveform (**c**) and the OBP waveform (**d**). In **b**–**d**, black dashed line represents the tsunami arrival time. Note that the location of the 52404 station as of the 2015 earthquake has been shifted by ~20 km southward from the location as of the 2008 earthquake (see text and Figure S8).

References

Albuquerque Seismological Laboratory (ASL)/USGS. (1992). IC: New China Digital Seismograph Network. https://doi.org/10.7914/SN/IC

Albuquerque Seismological Laboratory/USGS. (2014). IU: Global Seismograph Network (GSN - IRIS/USGS). https://doi.org/10.7914/SN/IU

Amelung, F., Jónsson, S., Zebker, H., & Segall, P. (2000). Widespread uplift and 'trapdoor' faulting on Galápagos volcanoes observed with radar interferometry. *Nature*, *407*(6807), 993–996. https://doi.org/10.1038/35039604

Anderson, K. R., Johanson, I. A., Patrick, M. R., Gu, M., Segall, P., Poland, M. P., et al. (2019). Magma reservoir failure and the onset of caldera collapse at Kīlauea Volcano in 2018. *Science*, *366*(6470). https://doi.org/10.1126/science.aaz1822

Baba, T., Takahashi, N., Kaneda, Y., Ando, K., Matsuoka, D., & Kato, T. (2015). Parallel Implementation of Dispersive Tsunami Wave Modeling with a Nesting Algorithm for the 2011 Tohoku Tsunami. *Pure and Applied Geophysics*, *172*(12), 3455–3472. https://doi.org/10.1007/s00024-015-1049-2

Bell, A. F., Hernandez, S., La Femina, P. C., & Ruiz, M. C. (2021). Uplift and seismicity driven by magmatic inflation at Sierra Negra volcano, Galápagos islands. *Journal of Geophysical Research, [Solid Earth]*, *126*(7). https://doi.org/10.1029/2021jb022244

Bernard, E. N., & Meinig, C. (2011). History and future of deep-ocean tsunami measurements. In *OCEANS'11 MTS/IEEE KONA* (pp. 1–7). ieeexplore.ieee.org. https://doi.org/10.23919/OCEANS.2011.6106894

Borrero, J. C., Cronin, S. J., Latu'ila, F. H., Tukuafu, P., Heni, N., Tupou, A. M., et al. (2023). Tsunami Runup and Inundation in Tonga from the January 2022 Eruption of Hunga Volcano. *Pure and Applied Geophysics*, *180*(1), 1–22. https://doi.org/10.1007/s00024-022-03215-5

Cabaniss, H. E., Gregg, P. M., Nooner, S. L., & Chadwick, W. W., Jr. (2020). Triggering of eruptions at Axial Seamount, Juan de Fuca Ridge. *Scientific Reports*, *10*(1), 10219. https://doi.org/10.1038/s41598-020-67043-0

Cesca, S., Letort, J., Razafindrakoto, H. N. T., Heimann, S., Rivalta, E., Isken, M. P., et al. (2020). Drainage of a deep magma reservoir near Mayotte inferred from seismicity and deformation. *Nature Geoscience*, *13*(1), 87–93. https://doi.org/10.1038/s41561-019-0505-5

Chikasada, N. Y. (2019). Short-wavelength Tsunami Observation Using Deep Ocean Bottom Pressure Gauges. In *The 29th International Ocean and Polar Engineering Conference*. International Society of Offshore and Polar Engineers. Retrieved from https://onepetro.org/conference-paper/ISOPE-I-19-707

Cole, J. W., Milner, D. M., & Spinks, K. D. (2005). Calderas and caldera structures: a review. *Earth-Science Reviews*, *69*(1), 1–26. https://doi.org/10.1016/j.earscirev.2004.06.004

Conder, J. (2019). focalmech(fm, centerX, centerY, diam, varargin) [Software]. MATLAB Central File Exchange. https://www.mathworks.com/matlabcentral/fileexchange/61227-focalmech-fm-centerx-centery-diam-varargin

Day, S. J. (2015). Chapter 58 - Volcanic Tsunamis. In H. Sigurdsson (Ed.), *The Encyclopedia of Volcanoes (Second Edition)* (pp. 993–1009). Amsterdam: Academic Press. https://doi.org/10.1016/B978-0-12-385938-9.00058-4

Duputel, Z., Rivera, L., Kanamori, H., & Hayes, G. (2012). W phase source inversion for moderate to large earthquakes (1990–2010). *Geophysical Journal International*, *189*(2), 1125–1147. https://doi.org/10.1111/j.1365-246X.2012.05419.x

Ekström, G., Nettles, M., & Dziewoński, A. M. (2012). The global CMT project 2004–2010: Centroid-moment tensors for 13,017 earthquakes. *Physics of the Earth and Planetary Interiors*, *200-201*, 1–9. https://doi.org/10.1016/j.pepi.2012.04.002

Eshelby, J. D. (1957). The Determination of the Elastic Field of an Ellipsoidal Inclusion, and Related Problems. *Proceedings of the Royal Society of London. Series A, Mathematical and Physical Sciences*, *241*(1226), 376–396. Retrieved from http://www.jstor.org/stable/100095

Fukao, Y., Sandanbata, O., Sugioka, H., Ito, A., Shiobara, H., Watada, S., & Satake, K. (2018). Mechanism of the 2015 volcanic tsunami earthquake near Torishima, Japan. *Science Advances*, *4*(4), eaao0219. https://doi.org/10.1126/sciadv.aao0219

Geist, D. J., Harpp, K. S., Naumann, T. R., Poland, M., Chadwick, W. W., Hall, M., & Rader, E. (2008). The 2005 eruption of Sierra Negra volcano, Galápagos, Ecuador. *Bulletin of Volcanology*, *70*(6), 655–673. https://doi.org/10.1007/s00445-007-0160-3

Geoware. (2011). TTT (Tsunami Travel Times) [Software]. Geoware Tsunami Product List. https://www.geoware-online.com/tsunami.html

Glastonbury-Southern, E., Winder, T., White, R. S., & Brandsdóttir, B. (2022). Ring fault slip reversal at bárðarbunga volcano, Iceland: Seismicity during caldera collapse and re‐inflation 2014–2018. *Geophysical Research Letters*, *49*(21). https://doi.org/10.1029/2021gl097613

Gregg, P. M., de Silva, S. L., Grosfils, E. B., & Parmigiani, J. P. (2012). Catastrophic caldera-forming eruptions: Thermomechanics and implications for eruption triggering and maximum caldera dimensions on Earth. *Journal of Volcanology and Geothermal Research*, *241–242*, 1–12. https://doi.org/10.1016/j.jvolgeores.2012.06.009

Gregg, P. M., Le Mével, H., Zhan, Y., Dufek, J., Geist, D., & Chadwick, W. W., Jr. (2018). Stress triggering of the 2005 eruption of Sierra Negra volcano, Galápagos. *Geophysical Research Letters*, *45*(24), 13288–13297. https://doi.org/10.1029/2018gl080393

Gregg, P. M., Zhan, Y., Amelung, F., Geist, D., Mothes, P., Koric, S., & Yunjun, Z. (2022). Forecasting mechanical failure and the 26 June 2018 eruption of Sierra Negra Volcano, Galápagos, Ecuador. *Science Advances*, *8*(22), eabm4261. https://doi.org/10.1126/sciadv.abm4261

Grilli, S. T., Tappin, D. R., Carey, S., Watt, S. F. L., Ward, S. N., Grilli, A. R., et al. (2019). Modelling of the tsunami from the December 22, 2018 lateral collapse of Anak Krakatau volcano in the Sunda Straits, Indonesia. *Scientific Reports*, *9*(1), 11946. https://doi.org/10.1038/s41598-019-48327-6

Gudmundsson, M. T., Jónsdóttir, K., Hooper, A., Holohan, E. P., Halldórsson, S. A., Ófeigsson, B. G., et al. (2016). Gradual caldera collapse at Bárdarbunga volcano, Iceland, regulated by lateral magma outflow. *Science*, *353*(6296), aaf8988. https://doi.org/10.1126/science.aaf8988

Hardebeck, J. L., & Okada, T. (2018). Temporal stress changes caused by earthquakes: A review. *Journal of Geophysical Research, [Solid Earth]*, *123*(2), 1350–1365. https://doi.org/10.1002/2017jb014617

Hasegawa, A., Yoshida, K., & Okada, T. (2011). Nearly complete stress drop in the 2011 Mw 9.0 off the Pacific coast of Tohoku Earthquake. *Earth, Planets and Space*, *63*(7), 35. https://doi.org/10.5047/eps.2011.06.007

Hayes, G. P., Rivera, L., & Kanamori, H. (2009). Source Inversion of the W-Phase: Real-time Implementation and Extension to Low Magnitudes. *Seismological Research Letters*, *80*(5), 817-822. https://doi.org/10.1785/gssrl.80.5.817

Heidarzadeh, M., Ishibe, T., Sandanbata, O., Muhari, A., & Wijanarto, A. B. (2020). Numerical modeling of the subaerial landslide source of the 22 December 2018 Anak Krakatoa volcanic tsunami, Indonesia. *Ocean Engineering*, *195*, 106733. https://doi.org/10.1016/j.oceaneng.2019.106733

Heidarzadeh, M., Putra, P. S., Nugroho, S. H., & Rashid, D. B. Z. (2020). Field Survey of Tsunami Heights and Runups Following the 22 December 2018 Anak Krakatau Volcano Tsunami, Indonesia. *Pure and Applied Geophysics*, *177*(10), 4577–4595. https://doi.org/10.1007/s00024-020-02587-w

Hjörleifsdóttir, V., & Ekström, G. (2010). Effects of three-dimensional Earth structure on CMT earthquake parameters. *Physics of the Earth and Planetary Interiors*, *179*(3), 178–190. https://doi.org/10.1016/j.pepi.2009.11.003

Japan Hydrographic Association. (2022). M7000 Digital Bathymetric Chart (ASCII file) [D7023A-2] [Dataset]. Japan Nautical Chart Web Shop. https://www.jha.or.jp/shop/index.php?main_page=product_info_js2&products_id=1409

Japan Hydrographic Association. (2011). Grid Bathymetric Data (JTOPO30v2) [Dataset]. Japan Nautical Chart Web Shop. https://www.jha.or.jp/shop/index.php?main_page=advanced_search_result&categories_id=1302

Japan Meteorological Agency. (2013). 73. Funka Asane. *National Catalogue of the active volcanoes in Japan (The forth edition)*. Retrieved from https://www.data.jma.go.jp/vois/data/tokyo/STOCK/souran_eng/volcanoes/073_funka_asane.pdf

Japan Meteorological Agency. (2022). Historical Activity of Funka Asane (in Japanese). Retrieved November 22, 2023, from https://www.data.jma.go.jp/vois/data/tokyo/328_FunkaAsane/328_history.html

Jónsson, S. (2009). Stress interaction between magma accumulation and trapdoor faulting on Sierra Negra volcano, Galápagos. *Tectonophysics*, *471*(1), 36–44. https://doi.org/10.1016/j.tecto.2008.08.005

Kajiura, K. (1963). The Leading Wave of a Tsunami. *Bulletin of the Earthquake Research Institute, University of Tokyo*, *41*(3), 535–571. Retrieved from https://ci.nii.ac.jp/naid/120000866529/

Kanamori, H., & Given, J. W. (1981). Use of long-period surface waves for rapid determination of earthquake-source parameters. *Physics of the Earth and Planetary Interiors*, *27*(1), 8–31. https://doi.org/10.1016/0031-9201(81)90083-2

Kanamori, H., & Rivera, L. (2008). Source inversion of Wphase: speeding up seismic tsunami warning. *Geophysical Journal International*, *175*(1), 222–238. https://doi.org/10.1111/j.1365-246X.2008.03887.x

Kilbride, B. M., Edmonds, M., & Biggs, J. (2016). Observing eruptions of gas-rich compressible magmas from space. *Nature Communications*, *7*, 13744. https://doi.org/10.1038/ncomms13744

Kubo, H., Kubota, T., Suzuki, W., Aoi, S., Sandanbata, O., Chikasada, N., & Ueda, H. (2022). Ocean-wave phenomenon around Japan due to the 2022 Tonga eruption observed by the wide and dense ocean-bottom pressure gauge networks. *Earth, Planets and Space*, *74*(1), 1–11. https://doi.org/10.1186/s40623-022-01663-w

Kubota, T., Saito, T., & Nishida, K. (2022). Global fast-traveling tsunamis driven by atmospheric Lamb waves on the 2022 Tonga eruption. *Science*, *377*(6601), 91–94. https://doi.org/10.1126/science.abo4364

Lai, V. H., Zhan, Z., Brissaud, Q., Sandanbata, O., & Miller, M. S. (2021). Inflation and asymmetric collapse at kīlauea summit during the 2018 eruption from seismic and infrasound analyses. *Journal of Geophysical Research, [Solid Earth]*. https://doi.org/10.1029/2021jb022139

Le Mével, H., Gregg, P. M., & Feigl, K. L. (2016). Magma injection into a long-lived reservoir to explain geodetically measured uplift: Application to the 2007-2014 unrest episode at Laguna del Maule volcanic field, Chile. *Journal of Geophysical Research, [Solid Earth]*, *121*(8), 6092–6108. https://doi.org/10.1002/2016JB013066

Lynett, P., McCann, M., Zhou, Z., Renteria, W., Borrero, J., Greer, D., et al. (2022). Diverse tsunamigenesis triggered by the Hunga Tonga-Hunga Ha'apai eruption. *Nature*, *609*(7928), 728–733. https://doi.org/10.1038/s41586-022-05170-6

Massa, B., D'Auria, L., Cristiano, E., & De Matteo, A. (2016). Determining the Stress Field in Active Volcanoes Using Focal Mechanisms. *Frontiers of Earth Science in China*, *4*. https://doi.org/10.3389/feart.2016.00103

Metz, D., Watts, A. B., Grevemeyer, I., Rodgers, M., & Paulatto, M. (2016). Ultra‐long‐range hydroacoustic observations of submarine volcanic activity at Monowai, Kermadec Arc. *Geophysical Research Letters*, *43*(4), 1529–1536. https://doi.org/10.1002/2015gl067259

Michon, L., Staudacher, T., Ferrazzini, V., Bachèlery, P., & Marti, J. (2007). April 2007 collapse of Piton de la Fournaise: A new example of caldera formation. *Geophysical Research Letters*, *34*(21). https://doi.org/10.1029/2007gl031248

Moyer, P. A., Boettcher, M. S., Bohnenstiehl, D. R., & Abercrombie, R. E. (2020). Crustal strength variations inferred from earthquake stress drop at axial seamount surrounding the 2015 eruption. *Geophysical Research Letters*, *47*(16). https://doi.org/10.1029/2020gl088447

Muhari, A., Heidarzadeh, M., Susmoro, H., Nugroho, H. D., Kriswati, E., Supartoyo, et al. (2019). The December 2018 Anak Krakatau Volcano Tsunami as Inferred from Post-Tsunami Field Surveys and Spectral Analysis. *Pure and Applied Geophysics*, *176*(12), 5219–5233. https://doi.org/10.1007/s00024-019-02358-2

Mulia, I. E., Watada, S., Ho, T.-C., Satake, K., Wang, Y., & Aditiya, A. (2020). Simulation of the 2018 tsunami due to the flank failure of anak krakatau volcano and implication for future observing systems. *Geophysical Research Letters*, *47*(14), e2020GL087334. https://doi.org/10.1029/2020gl087334

National Oceanic and Atmospheric Administration. (2005). Deep-ocean assessment and reporting of tsunamis (DART) [Dataset]. National Geophysical Data Center, NOAA. https://doi.org/10.7289/V5F18WNS

National Research Institute for Earth Science and Disaster Resilience. (2019). NIED F-net [Dataset]. National Research Institute for Earth Science and Disaster Resilience. https://doi.org/10.17598/NIED.0005

Newman, A. V., Dixon, T. H., & Gourmelen, N. (2006). A four-dimensional viscoelastic deformation model for Long Valley Caldera, California, between 1995 and 2000. *Journal of Volcanology and Geothermal Research*, *150*(1), 244–269. https://doi.org/10.1016/j.jvolgeores.2005.07.017

Nikkhoo, M., & Walter, T. R. (2015). Triangular dislocation: an analytical, artefact-free solution. *Geophysical Journal International*, *201*(2), 1119–1141. https://doi.org/10.1093/gji/ggv035

Peregrine, D. H. (1972). Equations for Water Waves and the Approximation behind Them. In R. E. Meyer (Ed.), *Waves on Beaches and Resulting Sediment Transport* (pp. 95–121). Academic Press. https://doi.org/10.1016/B978-0-12-493250-0.50007-2

Pritchard, M. E., Ji, C., & Simons, M. (2006). Distribution of slip from 11 $M_w > 6$ earthquakes in the northern Chile subduction zone. *Journal of Geophysical Research*, *111*(B10). https://doi.org/10.1029/2005jb004013

Purkis, S. J., Ward, S. N., Fitzpatrick, N. M., Garvin, J. B., Slayback, D., Cronin, S. J., et al. (2023). The 2022 Hunga-Tonga megatsunami: Near-field simulation of a once-in-a-century event. *Science Advances*, *9*(15), eadf5493. https://doi.org/10.1126/sciadv.adf5493

Riel, B., Milillo, P., Simons, M., Lundgren, P., Kanamori, H., & Samsonov, S. (2015). The collapse of Bárðarbunga caldera, Iceland. *Geophysical Journal International*, *202*(1), 446–453. https://doi.org/10.1093/gji/ggv157

Rodríguez-Cardozo, F., Hjörleifsdóttir, V., Jónsdóttir, K., Iglesias, A., Franco, S. I., Geirsson, H., et al. (2021). The 2014–2015 complex collapse of the Bárðarbunga caldera, Iceland, revealed by seismic moment tensors. *Journal of Volcanology and Geothermal Research*, 107275. https://doi.org/10.1016/j.jvolgeores.2021.107275

Ross, Z. E., Kanamori, H., & Hauksson, E. (2017). Anomalously large complete stress drop during the 2016M_w5.2 Borrego Springs earthquake inferred by waveform modeling and near‐source aftershock deficit. *Geophysical Research Letters*, *44*(12), 5994–6001. https://doi.org/10.1002/2017gl073338

Saito, T., Matsuzawa, T., Obara, K., & Baba, T. (2010). Dispersive tsunami of the 2010 Chile earthquake recorded by the high-sampling-rate ocean-bottom pressure gauges. *Geophysical Research Letters*, *37*(23). https://doi.org/10.1029/2010gl045290

Saito, T., Noda, A., Yoshida, K., & Tanaka, S. (2018). Shear strain energy change caused by the interplate coupling along the Nankai trough: An integration analysis using stress tensor inversion and slip-deficit inversion. *Journal of Geophysical Research, [Solid Earth]*, *123*(7), 5975–5986. https://doi.org/10.1029/2018jb015839

Sandanbata, O., Watada, S., Satake, K., Fukao, Y., Sugioka, H., Ito, A., & Shiobara, H. (2018). Ray Tracing for Dispersive Tsunamis and Source Amplitude Estimation Based on Green's Law: Application to the 2015 Volcanic Tsunami Earthquake Near Torishima, South of Japan. *Pure and Applied Geophysics*, *175*(4), 1371–1385. https://doi.org/10.1007/s00024-017-1746-0

Sandanbata, O., Kanamori, H., Rivera, L., Zhan, Z., Watada, S., & Satake, K. (2021). Moment tensors of ring-faulting at active volcanoes: Insights into vertical‐CLVD earthquakes at the Sierra Negra caldera, Galápagos islands. *Journal of Geophysical Research, [Solid Earth]*, *126*(6), e2021JB021693. https://doi.org/10.1029/2021jb021693

Sandanbata, O., & Saito, T. (2023). Quantifying magma overpressure beneath a submarine caldera: A mechanical modeling approach to tsunamigenic trapdoor faulting near Kita-Ioto Island, Japan [Dataset]. Zenodo. https://doi.org/10.5281/zenodo.8344070

Sandanbata, O., Watada, S., Ho, T.-C., & Satake, K. (2021). Phase delay of short-period tsunamis in the density-stratified compressible ocean over the elastic Earth. *Geophysical Journal International*, *226*(3), 1975–1985. https://doi.org/10.1093/gji/ggab192

Sandanbata, O., Watada, S., Satake, K., Kanamori, H., Rivera, L., & Zhan, Z. (2022). Sub‐decadal volcanic tsunamis due to submarine trapdoor faulting at Sumisu caldera in the Izu–Bonin arc. *Journal of Geophysical Research, [Solid Earth]*, *127*(9). https://doi.org/10.1029/2022jb024213

Sandanbata, O., Watada, S., Satake, K., Kanamori, H., & Rivera, L. (2023). Two volcanic tsunami events caused by trapdoor faulting at a submerged caldera near Curtis and Cheeseman islands in the Kermadec arc. *Geophysical Research Letters*, *50*(7). https://doi.org/10.1029/2022gl101086

Saurel, J.-M., Jacques, E., Aiken, C., Lemoine, A., Retailleau, L., Lavayssière, A., et al. (2021). Mayotte seismic crisis: building knowledge in near real-time by combining land and ocean-bottom seismometers, first results. *Geophysical Journal International*, *228*(2), 1281–1293. https://doi.org/10.1093/gji/ggab392

Scripps Institution of Oceanography. (1986). II: Global Seismograph Network - IRIS/IDA. https://doi.org/10.7914/SN/II

Segall, P., & Anderson, K. (2021). Repeating caldera collapse events constrain fault friction at the kilometer scale. *Proceedings of the National Academy of Sciences of the United States of America*, *118*(30). https://doi.org/10.1073/pnas.2101469118

Shelly, D. R., & Thelen, W. A. (2019). Anatomy of a caldera collapse: Kīlauea 2018 summit seismicity sequence in high resolution. *Geophysical Research Letters*, *46*(24), 14395–14403. https://doi.org/10.1029/2019gl085636

Shreve, T., & Delgado, F. (2023). Trapdoor fault activation: A step towards caldera collapse at Sierra Negra, Galápagos, Ecuador. *Journal of Geophysical Research, [Solid Earth]*. https://doi.org/10.1029/2023jb026437

Sparks, R. S. J. (2003). Forecasting volcanic eruptions. *Earth and Planetary Science Letters*, *210*(1), 1–15. https://doi.org/10.1016/S0012-821X(03)00124-9

Sugioka, H., Fukao, Y., Okamoto, T., & Kanjo, K. (2001). Detection of shallowest submarine seismicity by acoustic coupled shear waves. *Journal of Geophysical Research*, *106*(B7), 13485–13499. https://doi.org/10.1029/2000jb900476

Tepp, G., & Dziak, R. P. (2021). The Seismo-Acoustics of Submarine Volcanic Eruptions. *Journal of Geophysical Research, [Solid Earth]*, *126*(4), e2020JB020912. https://doi.org/10.1029/2020JB020912

Wang, T. A., Coppess, K. R., Segall, P., Dunham, E. M., & Ellsworth, W. (2022). Physics‐based model reconciles caldera collapse induced static and dynamic ground motion: Application to kīlauea 2018. *Geophysical Research Letters*, *49*(8). https://doi.org/10.1029/2021gl097440

Wang, T. A., Segall, P., Hotovec-Ellis, A. J., Anderson, K. R., & Cervelli, P. F. (2023). Ring fault creep drives volcano-tectonic seismicity during caldera collapse of Kīlauea in 2018. *Earth and Planetary Science Letters*, *618*, 118288. https://doi.org/10.1016/j.epsl.2023.118288

Wang, Y., Satake, K., Sandanbata, O., Maeda, T., & Su, H. (2019). Tsunami data assimilation of cabled ocean bottom pressure records for the 2015 torishima volcanic tsunami earthquake. *Journal of Geophysical Research, [Solid Earth]*, *124*(10), 10413–10422. https://doi.org/10.1029/2019jb018056

Wells, D. L., & Coppersmith, K. J. (1994). New Empirical Relationships among Magnitude, Rupture Length, Rupture Width, Rupture Area, and Surface Displacement. *Bulletin of the*

Seismological Society of America, *84*(4), 974–1002. https://doi.org/10.1785/BSSA0840040974

Ye, L., Kanamori, H., Rivera, L., Lay, T., Zhou, Y., Sianipar, D., & Satake, K. (2020). The 22 December 2018 tsunami from flank collapse of Anak Krakatau volcano during eruption. *Science Advances*, *6*(3), eaaz1377. https://doi.org/10.1126/sciadv.aaz1377

Zhan, Y., & Gregg, P. M. (2019). How accurately can we model magma reservoir failure with uncertainties in host rock rheology? *Journal of Geophysical Research, [Solid Earth]*, *124*(8), 8030–8042. https://doi.org/10.1029/2019jb018178

Zheng, Y., Blackstone, L., & Segall, P. (2022). Constraints on absolute magma chamber volume from geodetic measurements of trapdoor faulting at Sierra Negra volcano, Galapagos. *Geophysical Research Letters*, *49*(5). https://doi.org/10.1029/2021gl095683

References From the Supporting Information

Aki, K., & Richards, P. G. (1980). *Quantitative seismology: theory and methods* (Vol. 842). Freeman San Francisco, CA.

Dziewonski, A. M., & Anderson, D. L. (1981). Preliminary reference Earth model. *Physics of the Earth and Planetary Interiors*, *25*(4), 297–356. https://doi.org/10.1016/0031-9201(81)90046-7

Kawakatsu, H., & Yamamoto, M. (2015). 4.15 - Volcano Seismology. In G. Schubert (Ed.), *Treatise on Geophysics (Second Edition)* (pp. 389–419). Oxford: Elsevier. https://doi.org/10.1016/B978-0-444-53802-4.00081-6

Takeuchi, H., & Saito, M. (1972). Seismic surface waves. *Methods in Computational Physics*, *11*, 217–295.